A pressure-temperature phase diagram for zircon at extreme conditions

Nicholas E. Timms[1, 2], Timmons M. Erickson[1,2], Mark A. Pearce[3], Aaron J. Cavosie[1,2,4], Martin Schmieder[2,5,6], Eric Tohver[6], Steven M. Reddy[1,2], Michael R. Zanetti[7], Alexander A. Nemchin[1,2], and Axel Wittmann[8]*

[1] *Department of Applied Geology, The Institute for Geoscience Research, Curtin University, GPO Box U1987, Perth, WA 6845, Australia*

[2] *NASA Solar System Exploration Research Virtual Institute (SSERVI) Australia.*

[3] *CSIRO Mineral Resources, Australian Resources Research Centre, 26 Dick Perry Avenue, Kensington, WA 6151, Australia*

[4] *NASA Astrobiology Institute, Department of Geoscience, University of Wisconsin-Madison, Madison, Wisconsin 53706, USA*

[5] *Lunar and Planetary Institute, Houston, TX, USA*

[6] *School of Earth and Environment, University of Western Australia, 35 Stirling Highway, Crawley, WA 6009, Australia*

[7] *University of Western Ontario, 1151 Richmond St, London, Ontario, N6A 5B7, Canada*

[8] *Arizona State University, Tempe, AZ 85287, USA.*

*Corresponding author: n.timms@curtin.edu.au

Abstract

Hypervelocity impact processes are uniquely capable of generating shock metamorphism, which causes mineralogical transformations and deformation that register pressure (P) and temperature (T) conditions far beyond even the most extreme conditions created by terrestrial tectonics. The mineral zircon ($ZrSiO_4$) responds to shock deformation is various ways, including crystal-plasticity, twinning, polymorphism (*e.g.*, transformation to the isochemical mineral reidite), formation of granular texture, and dissociation to ZrO_2 + SiO_2, which provide robust thermobarometers that record different extreme conditions. The importance of understanding these material processes is two-fold. First, these processes can mobilize and redistribute trace elements, and thus be accompanied by variable degrees of resetting of the U-Pb system, which is significant for the use of zircon as a geochronometer. Second, some features described herein form exclusively during shock events and are diagnostic criteria that can be used to confirm the hypervelocity origin of suspected impact structures. We present new P-T diagrams showing the phase relations of $ZrSiO_4$ polymorphs and associated dissociation products under extreme conditions using available empirical and theoretical constraints. We present case studies to illustrate zircon microstructures formed in extreme environments, and present electron backscatter diffraction data for grains from three impact structures (Mistastin Lake of Canada, Ries of Germany, and Acraman of Australia) that preserve different minerals and microstructures associated with different shock conditions. For each locality, we demonstrate how systematic crystallographic orientation relationships within and between minerals can be used in conjunction with the new phase diagrams to constrain the P-T history. We outline a conceptual framework for a zircon-based approach to 'extreme thermobarometry' that incorporates both direct

observation of high-P and high-T phases, as well as inferences for the former existence of phases from orientation relationships in recrystallised products, a concept we refer to here as 'phase heritage'. This new approach can be used to unravel the pressure-temperature history of zircon-bearing samples that have experienced extreme conditions, such as rocks that originated in the Earth's mantle, and those shocked during impact events on Earth and other planetary bodies.

Keywords: Zircon, reidite, dissociation, EBSD, granular texture, shock, impact, zirconia, phase heritage

1. Introduction

Zircon ($ZrSiO_4$) is a common and durable mineral that is perhaps the most widely studied accessory phase because it can record geological events throughout deep time (e.g., Wilde et al., 2001; Valley et al., 2005; Hawkesworth and Kemp, 2006; Nemchin et al., 2009). However, zircon is not impervious in all environments, and can deform by various mechanisms as well as undergo phase transformations, especially at extreme pressure and temperature conditions, beyond so-called 'ultra-high pressure' and 'ultra-high temperature' metamorphic conditions found in the Earth's crust (e.g., Hacker et al., 1998; Harley et al., 2007; Korhonen et al., 2013; Korhonen et al., 2014; Clark et al., 2015) or those that can be achieved during seismic events along tectonic faults (e.g., Wenk and Weiss, 1982; Di Toro and Pennacchioni, 2004). Environments where zircon experiences extreme conditions include the lithospheric mantle, such as during kimberlite eruption, and also hypervelocity impact events on Earth, the Moon, and other planetary bodies. Zircon can undergo brittle fracture and cataclasis (e.g., Boullier, 1980; Corfu et al., 2003; Rimša et al., 2007), crystal-plasticity via formation and migration of dislocations (e.g., Reimold et al., 2002; Reddy et al., 2006; Moser et al., 2009; Reddy et al., 2009; Timms et al., 2012b), mechanical twinning (e.g., Moser et al., 2011; Timms et al., 2012b; Erickson et al., 2013a; Thomson et al., 2014; Erickson et al., 2016; Montalvo et al., in press), and solid-state recrystallization via nucleation and growth of neoblasts (e.g., Piazolo et al., 2012; Cavosie et al., 2015b). Zircon can also transform to reidite, a high-pressure $ZrSiO_4$ polymorph (e.g., Glass and Liu, 2001; Gucsik et al., 2002; Wittmann et al., 2006; Cavosie et al., 2015a; Reddy et al., 2015), and undergo dissociation to zirconia (ZrO_2) and silica (SiO_2) (Fig. 1) (e.g., El Goresy, 1965; Zanetti, 2015). The presence of twins and reidite in zircon are interpreted to be diagnostic of high-pressure shock deformation, and have been

used as evidence of hypervelocity impact (e.g. Cavosie et al., 2015a; Reddy et al., 2015). Zircon from impact settings can also preserve a distinctive microporosity (e.g., Wittmann et al., 2006; Grange et al., 2013a; Schmieder et al., 2015; Singleton et al., 2015), form diaplectic glass (e.g., Leroux et al., 1999; Wittmann et al., 2006), and even form a fluidal-vesicular texture reminiscent of devolatilised glass (e.g., Hamann et al., in press).

The U-Pb system in zircon can be modified during all of the deformation, recrystallisation and transformation processes described above to varying degrees. Migration of Pb into clusters at the 10 nm scale during thermal events can result in both concordant and discordant U-Pb isotopic data when measured at the 20 μm scale (Valley et al., 2014; Peterman et al., 2016). Crystal-plastic deformation generates fast-diffusion pathways that can mobilise U, Th, Pb and other trace elements at relatively modest temperatures (e.g., Reddy et al., 2006; Timms et al., 2006; Timms et al., 2011; Peterman et al., 2016; Piazolo et al., 2016; Reddy et al., 2016; Tretiakova et al., 2016). If deformation occurs soon after crystallisation yet before appreciable radiogenic Pb has accumulated, then Pb-loss may not be detectable outside the uncertainties of secondary ion mass spectrometry (SIMS) analyses (e.g., Timms et al., 2006; Timms et al., 2011; Crow et al., 2015). Crystal-plasticity and twinning can result in no detectable Pb-loss (Erickson et al., 2013b; Cavosie et al., 2015b)}; partial Pb-loss yielding apparent ages with uncertain meaning (e.g., Deutsch, 1990; Deutsch and Schärer, 1990; Grange et al., 2013b); discordant arrays with a lower intercept corresponding to a deformation age (e.g., Krogh et al., 1993a; Moser, 1997; Moser et al., 2009; Moser et al., 2011; MacDonald et al., 2013); or locally complete U-Pb resetting to yield deformation ages (e.g., Moser et al., 2009; Nemchin et al., 2009; Grange et al., 2013b; Bellucci et al., 2016). Recrystallization (neoblast growth,

106 granular texture) can cause U-Pb resetting and can yield deformation ages (e.g.,
107 Krogh et al., 1993b; Kamo and Krogh, 1995; Grange et al., 2009; Moser et al., 2011;
108 Piazolo et al., 2012; Grange et al., 2013a; Cavosie et al., 2015b). However, U-Pb data
109 from granular zircon does not always yield reliable event ages. For example, where
110 neoblasts are too small to analyse via SIMS without contamination from surrounding
111 interstitial material or have experienced subsequent Pb-loss (e.g., Deloule et al., 2001;
112 Tohver et al., 2012; Schmieder et al., 2015). Similar effects of deformation
113 microstructures have been observed on the U-Th-Pb system in monazite (e.g.,
114 Deutsch and Schärer, 1990; Moser, 1997; Flowers et al., 2003; Tohver et al., 2012;
115 Erickson et al., 2015; Erickson et al., 2016; Erickson et al., in review). Therefore, it is
116 important to understand the systematic mechanical and thermodynamic behaviour of
117 zircon at extreme conditions.

118 Much attention has been given to the solubility (Ayers et al., 2012; Wilke et
119 al., 2012; Bernini et al., 2013) and saturation (Watson and Harrison, 1983; Boehnke et
120 al., 2013; Gervasoni et al., 2016) behaviour of zircon in melts and aqueous fluids.
121 However, these processes are fundamentally different to those discussed here because
122 at extreme temperature zircon undergoes solid state thermal dissociation to oxides
123 rather than melting congruently (Fig. 1) (Butterman and Foster, 1967; Kaiser et al.,
124 2008). While many aspects of the fate of zircon at extreme conditions have been
125 published, only a few studies have attempted to show how variations in pressure-
126 temperature (P-T) histories result in characteristic microstructures and phase relations
127 observed in natural zircon (Wittmann et al., 2006; Timms et al., 2012b; Singleton et
128 al., 2015). To date, no studies have incorporated all available experimental data for
129 polymorphism and dissociation of zircon, nor have all of the known microstructures

130 associated with these processes, which have been reported in natural samples from
131 extreme environments, been fully integrated.
132 The aim of this study is to develop a comprehensive conceptual framework for
133 interpreting zircon from extreme environments, with an emphasis on constraining P-T
134 conditions that explain formation of deformation microstructures, polymorphic
135 transformations, granular texture, and dissociation to zirconia and silica. This is
136 achieved in three ways. Firstly, we provide a new thermodynamic calculation
137 describing the zircon dissociation reaction and, along with published data, construct a
138 new P-T phase diagram for $ZrSiO_4$ and its related polymorphs and dissociation
139 products that are stable at extreme conditions (up to ~3000 °C and 40 GPa).
140 Secondly, we present three case studies of zircon from terrestrial meteorite impact
141 environments to illustrate microstructures and orientation relationships among phases
142 and better understand the behaviour of zircon during impact processes. Thirdly, we
143 interpret the three case studies within the framework of the new phase diagram to
144 demonstrate how orientation analysis of $ZrSiO_4$ and related phases can be used to
145 constrain the P-T paths experienced by zircon under extreme conditions.
146

147 **2. Approach, Materials and Methods**

148 Available data from laboratory experiments and *ab initio* simulations were compiled
149 as two sets of P-T phase diagrams – one type in which various transformations and
150 deformations of $ZrSiO_4$ are plotted, and another that illustrates $ZrSiO_4$ dissociation
151 reactions and the phase stability of ZrO_2 and SiO_2 dissociation products.

152 ***2.1 Available data for phase stability and deformation***

153 Data for the transformation of zircon (tetragonal, space group $I4_1/amd$) to reidite
154 (tetragonal, space group $I4_1/a$) has been sourced from *ab initio* calculations (Marqués

et al., 2006; Marqués et al., 2008; Du et al., 2012; Dutta and Mandal, 2012), static high-pressure laboratory experiments where temperature is constrained (Reid and Ringwood, 1969; Liu, 1979; Knittle and Williams, 1993; Ono et al., 2004a; Ono et al., 2004b; van Westrenen et al., 2004; Chaplot et al., 2006; Morozova, 2015), and shock deformation experiments where temperature is not constrained (Mashimo et al., 1983; Kusaba et al., 1985; Leroux et al., 1999). A 'post-reidite' $ZrSiO_4$ phase with wolframite structure (*P2/c*) has been predicted to exist above 75.8 GPa, but has not yet been produced in experiments (Dutta and Mandal, 2012) or observed in nature. Planar dislocations in zircon occur at 20 GPa in shock recovery experiments (Leroux et al., 1999). Twinning in zircon has been observed in diamond anvil experiments at 20 GPa (Morozova, 2015), and in reidite during shock experiments at 40 GPa (Leroux et al., 1999).

Dissociation of zircon to zirconia and silica has been constrained in laboratory experiments at ambient pressure (Fig. 1) (Butterman and Foster, 1967; Kaiser et al., 2008; Telle et al., 2015), and has also been observed in slag from smelting of tin ore (Farthing and Pivarunas, 2015; Cavosie et al., 2016c) and in fused bedrock at nuclear blast sites (Lussier et al., in press). The stabilities of dissociation products, including polymorphs of silica (SiO_2), such as α- and β-quartz, tridymite, cristobalite, coesite, stishovite, and liquid silica, are sourced from Swamy et al. (1994) and references therein (e.g., Fenner, 1913; Kennedy et al., 1962; Ostrovsky, 1966; Cohen and Klement, 1967; Jackson, 1976; Yagi and Akimoto, 1976; Suito, 1977; Grattan-Bellew, 1978; Mirwald and Massonne, 1980; Bohlen and Boettcher, 1982; Kanzaki, 1990; Pacalo and Gasparik, 1990; Zhang, 1992). The stability fields of several polymorphs of SiO_2 and ZrO_2 are not well defined. High pressure 'post-stishovite' SiO_2 polymorphs with $CaCl_2$- and α-PbO_2-like structures are stable above 48 and ~85

GPa, respectively (El Goresy et al., 2004). Transformation of silica into lechatelierite, which is a diaplectic phase that is commonly vesicular, can occur at extreme temperatures up to several thousand degrees (Kieffer et al., 1976; Macris et al., 2014; Cavosie et al., 2016b). High-pressure (>100 GPa) hexagonal and tetragonal ZrO_2 phases have been reported (Arashi et al., 1990; Ohtaka et al., 1994). However, these phases are not represented on the phase diagrams in this study.

The stability of zirconia polymorphs of zirconia, including monoclinic (baddeleyite), tetragonal, cubic, and two orthorhombic polymorphs, as well as liquid zirconia, are taken from Kaiser et al. (2008) and Bouvier et al. (2000) and references therein (e.g., Whitney, 1965; Block et al., 1985; Ohtaka et al., 1991; Ohtaka et al., 1994; Haines et al., 1995; Haines et al., 1997). Experimental dissociation of reidite has been documented by diamond anvil cell (Liu, 1979; Tange and Takahashi, 2004) and in shocked charges (Mashimo et al., 1983).

2.2 Thermodynamic calculation of the zircon dissociation reaction

The equilibrium breakdown of zircon to zirconia and silica (cristobalite) was extrapolated from the experimentally constrained temperature of 1938 °K (1665 °C) at 1 bar (1.01 x 10-4 GPa Kaiser et al., 2008) using available data (Table 1, Adams et al., 1985; Subbarao et al., 1990; Robie and Hemingway, 1995; Mittal et al., 1998; Mao et al., 2001; Bouvier et al., 2002; O'Neill, 2006; Ortiz et al., 2007). Thermodynamic expressions (O'Neill, 2006) for heat capacity were used to calculate high temperature entropy and enthalpy of formation. Thermal expansion data were used for calculation of molar volume as a function of temperature. The limited pressure range necessary for the calculation means that pressure dependence can be

204 neglected. Further details of the thermodynamic calculation can be found in Appendix
205 1.
206
207 ***2.3 Phase orientation relationships and their significance***
208 Deformation of and associated transformations among $ZrSiO_4$, ZrO_2, and SiO_2 phases
209 occur via systematic crystallographic orientation relationships. Established orientation
210 relationships include those associated with mechanical twinning and dislocation creep
211 in zircon (e.g., Timms et al., 2012b), transformation of zircon to reidite (e.g., Leroux
212 et al., 1999; Erickson et al., in press), and between low-P zirconia polymorphs (e.g.,
213 Chevalier et al., 2009; Cayron et al., 2010). Orientation analysis can yield information
214 about deformation mechanisms and phase changes that occur at extreme conditions
215 (e.g., Kerschhofer et al., 2000; Cavosie et al., 2016b). However, orientation
216 relationships associated with zircon dissociation, or among high-P zirconia
217 polymorphs have not been characterised. This study applies known orientation
218 relationships and identifies new relationships in three case studies to provide new
219 insight into deformation and transformation histories.
220 Crystal-plastic microstructures, including subgrains and planar deformation
221 bands (PDBs) with low-angle boundaries occur in samples that have experienced
222 deformation (e.g., Moser et al., 2009; Timms et al., 2012b; Erickson et al.,
223 2013a)Kovaleva, 2015 #296;Montalvo, in press #1242}, and so it is important to
224 account for their effects on crystallographic orientations in zircon crystals that have
225 experienced extreme conditions. Crystal-plastic deformation causes progressive,
226 incremental, low-angle dispersion of crystallographic directions, commonly with
227 angle/axis pairs that describe minimum misorientation (also known as disorientation)
228 between adjacent data points (c.f. Wheeler et al., 2001) that coincide with rational

low-index directions related to the operation of different dislocation slip systems (Reddy et al., 2006; Reddy et al., 2007; Kaczmarek et al., 2011; Timms et al., 2012a). The most commonly reported slips systems are {100}<010> or {001}<100> (Reddy et al., 2007; Nemchin et al., 2009; Reddy et al., 2009; Timms and Reddy, 2009; Kaczmarek et al., 2011; Piazolo et al., 2012; Timms et al., 2012b; MacDonald et al., 2013; Cavosie et al., 2015a; Kovaleva et al., 2015; Kovaleva et al., 2016).

Deformation twinning in zircon is readily distinguished from growth twinning (e.g., Jocelyn and Pidgeon, 1974), as it produces polysynthetic lamellar forms (Timms et al., 2012b; Erickson et al., 2013a). Twinning occurs along {112}, and twinned domains have a specific misorientation relationship of 65° around <110> of the host grain (Moser et al., 2011; Timms et al., 2012b; Erickson et al., 2013a; Cavosie et al., 2015a; Montalvo et al., in press). This misorientation relationship is consistent with the twin mode as K_1{112} η_1<111>, where K_1 is the composition plane and η_1 is the shear direction (Christian and Mahajan, 1995), and is consistent with impact-related twins in other tetragonal accessory phases (Cavosie et al., 2016a). Up to four distinct, symmetrically equivalent {112} twin orientations are possible in zircon (Erickson et al., 2013a; Cavosie et al., 2015b). Rare, non-lamellar, equant twinned domains at the intersection between planar deformation features have been reported in lunar zircon (Timms et al., 2012b).

The transformation of zircon to reidite can produce lamellar and granular forms. Lamellar reidite has been described with an approximate 90° / <110> disorientation relationship with the host zircon (Kusaba et al., 1985; Leroux et al., 1999; Cavosie et al., 2015a; Reddy et al., 2015). However, detailed 3D analyses have revealed that multiple sets of lamellae can form along a variety of non-rational habit planes in zircon (Reddy et al., 2015; Erickson et al., in press). The crystallographic

orientation relationship of reidite to the parent zircon was proposed to occur via alignment of $<110>_{zircon}$ to $<110>_{reidite}$ and $<001>_{zircon}$ to $<110>_{reidite}$ (Kusaba et al., 1985; Leroux et al., 1999). More recently, (Erickson et al., in press) have proposed that a $\{100\}_{zircon}$ is parallel to a $\{112\}_{reidite}$ and that both phases share a {112}. The tetragonal symmetry of both phases means that up to eight distinct reidite orientations can form in a single crystal of zircon, resulting in two main groups of reidite with four orientations in each group having similarly-oriented $(001)_{reidite}$ (Erickson et al., in press). Sub-micrometer diameter granular reidite has also been reported to coexist with lamellar reidite in zircon from the ~6 km-diameter Rock Elm (Wisconsin, USA) and ~24 km Ries (Germany) impact structures (Cavosie et al., 2015a; Erickson et al., in press). Granular reidite shares a similar yet less strictly adhered to misorientation relationship with zircon as lamellar reidite, resulting in a more broadly scattered orientation distribution (Cavosie et al., 2015a; Erickson et al., in press).

Various mechanisms for the zircon → reidite transformation have been proposed, and include a displacive (martensitic) transformation that involves shear along {100} with a [001] shear vector (Leroux et al., 1999); a quasi-displacive, two-stage transformation that involves partial dislocation along (100) followed by displacement of oxygen ions (Kusaba et al., 1986; Turner et al., 2014), and a reconstructive transformation that involves an intermediate monoclinic $ZrSiO_4$ phase (Marqués et al., 2008; Smirnov et al., 2008; Flórez et al., 2009). It has been shown via *ab initio* calculations that a reconstructive transformation is energetically favourable (Marqués et al., 2008; Smirnov et al., 2008; Flórez et al., 2009). Cavosie et al. (2015a) and Erickson et al. (in press) have argued that granular and lamellar reidite form by reconstructive and displacive mechanisms, respectively.

278 Under extreme P-T conditions, zircon can recrystallise into a granular texture
279 (e.g., Bohor et al., 1993; Kamo et al., 1996; Wittmann et al., 2006; Grange et al.,
280 2013a; Schmieder et al., 2015). Neoblasts in shock-deformed zircon nucleate in
281 orientations that are widely and non-systematically dispersed from the parent grain
282 orientation (e.g., Cavosie et al., 2015b), or systematically misoriented from one
283 another (Cavosie et al., 2016b). Individual zircon neoblasts in granular zircon grains
284 from Meteor Crater preserve ~65° / <110> and ~90° / <110> misorientations that are
285 interpreted to have nucleated from twinned domains and reverted from reidite,
286 respectively (Cavosie et al., 2016b).
287 Thermal dissociation of zircon at 1673 °C and ambient pressure produces
288 tetragonal zirconia and cristobalite, with the latter melting to form liquid SiO_2 with
289 only ~10 °C of further heating (Butterman and Foster, 1967; Kaiser et al., 2008). Due
290 to the absence of SiO_2 polymorphs with dissociated zircon, silica polymorphs
291 resulting from zircon dissociation are not generally preserved (Kaiser et al., 2008).
292 However, experiments suggest reidite dissociation may produce solid-state oxide
293 products, in which case stishovite should be the stable phase (e.g. , Tange and
294 Takahashi, 2004). Systematic crystallographic relations resulting from transformation
295 among zirconia polymorphs are well known from material science and ceramics
296 literature (e.g. , Smith and Newkirk, 1965; Bansal and Heuer, 1972; Subbarao et al.,
297 1974). Transformation of cubic to tetragonal zirconia is displacive but not martensitic
298 and can result in up to three possible distinct orientations whereby $(001)_{tetragonal}$ is
299 parallel to a $\{100\}_{cubic}$ (Heuer, 1987). The tetragonal to monoclinic ZrO_2
300 transformation is martensitic and can result in up to four distinct orientation variants
301 from each precursor tetragonal identity. Therefore, up to twelve monoclinic variants
302 can result from the two-stage cubic to monoclinic transformation, which can be used

303 to uniquely identify the existence and original orientation of the precursor cubic
304 polymorph that was stable at much higher temperature (Kerschhofer et al., 2000;
305 Cayron, 2007; Chevalier et al., 2009; Cayron et al., 2010; Humbert et al., 2010). A
306 transmission electron microscopy study of a baddeleyite megacryst from a kimberlite
307 identified the former existence of high-temperature ZrO_2 polymorphs using
308 crystallographic orientation relationships (Kerschhofer et al., 2000). However, this
309 concept has not yet been applied to studies involving zircon, and the crystallographic
310 orientation relationships between zircon and dissociated ZrO_2 phases remain
311 unknown.
312
313 ***2.4 Samples used for the case studies***
314 Zircon grains from three terrestrial meteorite impact structures were chosen for this
315 study. The first zircon grain is from the late Eocene, 37.83 ± 0.05 Ma, and ~28 km
316 diameter Mistastin Lake impact structure in northern Labrador, Canada (55º53' N;
317 63º18' W) (Grieve, 1975; Marion, 2009; Sylvester et al., 2013). The zircon is a clast
318 component in a holohyaline impact melt rock that was found as float on top of the 80
319 m thick Discovery Hill outcrop, which is a large columnar-jointed impact melt
320 outcrop near the crater wall (Marion and Sylvester, 2010). The sample has a dark
321 brown to black, non-vesicular glassy matrix, similar to obsidian, and contains sparse
322 sub-rounded mineral clasts, which are partially-digested remnants of the
323 Mesoproterozoic crystalline target rocks (primarily granodiorite, mangerite, and
324 anorthosite) (Fig. 2A). The zircon grain has a halo of Zr-enriched silicate glass that
325 forms a trail several millimeters long (Fig. 2B).
326 The second zircon specimen is from the 14.83 ± 0.15 Ma, 24 km diameter Ries
327 impact structure in Germany (Shoemaker and Chao, 1961; Di Vincenzo and Skála,

2009; Jourdan et al., 2012). The studied zircon grain is from a clast in suevite breccia recovered from a depth of 498 m in the Nördlingen 1973 borehole, which is located 3.65 km from the centre of the Ries impact structure (48°53' N, 10°37' E); (Bauberger et al., 1974; Stöffler, 1977; Reimold et al., 2011; Erickson et al., in press). The sample belongs to a melt-rich section of suevite inferred to be *Flädle*-bearing and deposited from the impact vapor plume, and possibly reworked within the impact crater (Stöffler, 1977; Meyer et al., 2011; Stöffler et al., 2013). The zircon is one of seven reidite-bearing grains in a clast of shocked Variscan basement gneiss containing maskelynite and amorphous SiO_2 (Fig. 2C). The presence of maskelynite and diaplectic quartz suggests that the clast experienced shock stage II conditions, with shock pressures of 35 - 45 GPa (Stöffler, 1971).

The third zircon specimen in this study is from the deeply eroded, ~600 Ma, ≥40 km-diameter Acraman impact structure in South Australia, where the target rocks are assigned to the Yardea Dacite of the Mesoproterozoic (~1.59-1.60 Ga) siliceous Gawler Range Volcanics (Williams, 1986; Williams, 1994; Allen et al., 2003; Allen et al., 2008; Schmieder et al., 2015). The sample in this study is from a ~12 x 3 m wide body of impact melt rock within the ~30 km diameter circular central domain defined by Lake Acraman, which is possibly a melt dike injected into the centrally-uplifted crater basement (32°3'20.3" S, 135°26'51.1" E). The melt rock is reddish and has a heterogeneously-developed albite-spinifex texture, and contains variable proportions of partially-digested relict clasts of Yardea Dacite (Fig. 2D) (Schmieder et al., 2015).

2.5 Analytical procedure

Petrographic slides of each sample were prepared for electron backscatter diffraction (EBSD) analysis (Prior et al., 1999), and electron microscopy was done using a Tescan MIRA3 field emission scanning electron microscope (FE-SEM) fitted with an Oxford Instruments AZtec combined energy dispersive X-ray (EDX) / EBSD acquisition system housed at the Microscopy and Microanalysis Facility, John de Laeter Centre, Curtin University, using established settings and protocols (Table 2) (Reddy et al., 2008; Cavosie et al., 2015a; Cavosie et al., 2015b; Reddy et al., 2015). Backscattered electron (BSE), cathodoluminescence (CL) images, EBSD and EDX maps with step sizes between 40 and 250 nm were collected from each grain. Indexing of EBSD patterns included a choice of match units for zircon, reidite and monoclinic, tetragonal, cubic and orthorhombic polymorphs of ZrO_2 (Table 2). Oxford Instruments' Channel 5.10 software was used to remove isolated, erroneous EBSD data points (wildspike correction), calculate disorientation angle/axis pairs between adjacent data points of the same phase (Wheeler et al., 2001), and produce thematic EBSD maps and pole figures (Timms et al., 2012b; Cavosie et al., 2015a; Reddy et al., 2015).

3. Results and Interpretation

3.1 Synthesis of phase diagrams for zircon at extreme P-T conditions

3.1.1 A pressure-temperature phase diagram for $ZrSiO_4$

Available empirical and experimental constraints, and equilibrium calculations on the conditions under which phase transformations of $ZrSiO_4$ occur are summarised in Figure 3, and discussed below.

3.1.2 Transformation of zircon to reidite

Static density functional theory (DFT) calculations (Marqués et al., 2006; Marqués et al., 2008; Dutta and Mandal, 2012) indicate ~ 5 GPa for the equilibrium thermodynamic phase transformation to reidite at hydrostatic pressure (Fig. 3A). A similar pressure has been observed experimentally for the zircon-type to scheelite-type structure transformation in orthovanadates (Yue et al., 2016). Significant discrepancies exist between theoretical predictions (5 GPa), static experiments (~12-23 GPa) and the appearance of reidite in shock experiments (~30 GPa). These differences may be attributed to the effects of an energy barrier to transformation associated with a transition state (Marqués et al., 2006) and/or kinetic effects (Fig. 3A). However, the nature of these effects on reidite formed during shock compression has yet to be investigated, and so the fields depicted in Fig. 3A serve as a first-order guide only. Nevertheless, all available studies indicate that transformation of zircon to reidite is highly pressure-dependent.

Defects in the zircon lattice can affect the transformation to reidite, which has significant implications for natural zircon with its abundant trace elements and ubiquitous radiation damage. For example, non-stoichiometry affects the transformation kinetics and compressibility of zircon (van Westrenen et al., 2004), and ion beam irradiated zircon transforms to reidite at much higher static pressures (~37 GPa) than non-irradiated zircon (Lang et al., 2008). This is consistent with observations in natural reidite-bearing zircon where non-cathodoluminescent, partially radiation-damaged domains do not contain reidite lamellae (Cavosie et al., 2015a; Reddy et al., 2015). Only recently have studies begun to systematically investigate the effects of radiation damage and non-stoichiometry on the conditions of reidite transformation in natural zircon (c.f., Erickson et al., in press; Timms et al., in review).

3.1.3 Mechanical twinning in zircon and reidite

Mechanical twinning is considered to be a structural transformation akin to a displacive (or martensitic) transformation (Christian and Mahajan, 1995). Few empirical constraints exist for twinning in zircon (Morozova, 2015) and reidite formation (Leroux et al., 1999; Morozova, 2015), and so experimentally determined minimum twinning pressures of 20 GPa and 40 GPa, respectively, are tentatively assigned for those processes (Fig. 3A). The effects of temperature on twin formation in zircon and reidite have yet to be evaluated.

3.1.4 Dissociation of zircon and reidite

The Clapeyron slope for the zircon breakdown reaction calculated here is on the order of 29 bar (2.9×10^{-3} GPa) / °C (Fig. 3B). This means that zircon breakdown is a low-P, high-T reaction that intersects the cristobalite solidus at ~1.4 kbar (~0.14 GPa) (Fig. 3Bii). However, the up-temperature continuation of the reaction line cannot be extrapolated with confidence due to undetermined thermodynamic effects of liquid silica on phase stability. Nevertheless, these results indicate that dissociation of zircon is essentially a high-T (~1690 °C), low-P process within the range of the calibration (Butterman and Foster, 1967; Kaiser et al., 2008). The effects of intrinsic radiation damage on zircon dissociation have not been well constrained. A lower dissociation temperature of ~1540 °C (Fig. 3Bii) for natural zircon at ambient pressure reported by Curtis and Sowman (1953) could potentially be attributed to the various defects discussed above being present in the natural zircon analysed.

There is currently insufficient thermodynamic data available for equilibrium calculation of the reidite dissociation reaction. However, ‘hydrostatic’ diamond anvil

427 cell experiments reveal that dissociation of reidite occurs above ~20-23 GPa in the
428 1500-1800 °C range (Tange and Takahashi, 2004). These results suggest that reidite
429 becomes unstable at high-P and low-T conditions, which is difficult to reconcile with
430 other available experimental constraints on reidite stability (Fig. 3A,B).
431
432 *3.1.5 A P-T phase diagram for zircon dissociation products*
433 The single-component phase diagrams for SiO_2 and ZrO_2 have been combined to
434 predict equilibrium stabilities for zircon dissociation products, assuming that ZrO_2
435 and SiO_2 behave independently at the conditions under consideration (Fig. 3B). The
436 predicted sequence of stable zirconia and silica polymorphs depends on the specific
437 P-T path followed, assuming that equilibrium can be achieved. However, it is
438 acknowledged that impedance of reaction kinetics due to rapid temperature and
439 pressure changes during impact events could result in preservation of metastable
440 phases. For further information on the effects of shock on SiO_2, readers are referred to
441 Schmitt and Ahrens (1989). Reversion of the oxides to $ZrSiO_4$ is only possible upon
442 re-entry of the stability fields of either zircon or reidite (Figs 1B, 3A, C), if kinetics
443 are favourable. However, if reversion is sluggish or incomplete, then a combination of
444 both the $ZrSiO_4$ and $ZrO_2 + SiO_2$ P-T phase diagrams is required to predict metastable
445 phases through P-T space (Figs 1 and 3).
446 One exception to the general application of these phase diagrams occurs in
447 thermally annealed radiation-damaged zircon, which can produce ~10 nm zirconia
448 crystals in silica glass at 1250 °C (e.g., McLaren et al., 1994). Metastable tetragonal
449 zirconia is strongly grain size-dependent, whereby crystals in the size range of 30-80
450 nm can grow at temperatures as low as 410 °C (Subbarao et al., 1974). Zirconia in
451 this size range has been reported in impact-dissociated zircon (Cavosie et al., 2016b),

highlighting the potential for discovery of natural occurrences of tetragonal zirconia as a result of impact processes.

3.2 Case Studies

3.2.1 Mistastin Lake zircon (impact glass)

The zircon grain from Mistastin Lake [MZRN-2 from Zanetti (2015)] is ~100-150 μm across and comprises an oscillatory zoned core and an intermediate zone containing zircon that is bright in CL and interspersed with elongate, ~500 nm wide baddeleyite grains and silica glass arranged in a radial pattern (Fig. 4A). The zircon core has a single crystallographic orientation and does not contain microstructures indicative of shock (Fig. 4A, D, E). The oscillatory zoning is interpreted to represent primary magmatic growth. Zircon in the intermediate zone preserves up to 2° disorientation from the zircon core (Fig. 4D). The grain is surrounded by a 10-20 μm wide corona of vermicular/dendritic baddeleyite with rounded boundaries, locally elongate at high angles to the zircon margin, and interspersed with silicate glass with a similar bulk composition as that outside the corona (Fig. 4B, C) (Zanetti, 2015). Irregular-shaped, 10-30 μm wide clusters of morphologically-similar baddeleyite are discernible within the corona (Fig. 4B-E).

All ZrO_2 grains index as baddeleyite and are pervasively twinned; no other zirconia or $ZrSiO_4$ polymorphs were detected in the corona by EBSD (Fig. 4). Each baddeleyite grain cluster contains twinned laths with up to twelve distinct crystallographic orientations that are systematically misoriented relative to one another and the host zircon (Fig. 4D-F). The twin boundaries between laths have the following misorientation relationships: 180° around <001>, <00-1>, <100>, <-100>,

476 <101> and <-10-1>; 115° around <1-1-1> and <-1-1-1>; and 90° around <104> and
477 <-10-4> (Fig. 4D).
478 Within each cluster, three approximately orthogonal groups of baddeleyite
479 orientations are present (Fig. 4E-F). Poles to {010} in each group coincide, whereas
480 poles to {100} and {010} are systematically distributed by ~20°, commonly
481 producing 'cross shapes' in pole figures (Fig. 4F). No consistent, systematic
482 orientation relationships between the host zircon and baddeleyite clusters were
483 observed.
484

485 ***3.2.2 Ries crater zircon (shocked target rock clast in suevite)***

486 The Ries zircon grain [grain 37 from Erickson et al. (in press)] is ~20 μm
487 across and comprises a non-luminescent core surrounded by an unevenly-developed
488 bright-CL rim (Fig. 5A). The core consists of a patchy distribution of sub-equant
489 domains (granules) with a mean diameter of 240 nm that variably index as zircon or
490 reidite, and abundant irregular fractures (Fig. 5B,C). Indexing is not possible
491 elsewhere in the core due to poor EBSD pattern quality. Poles for data points indexed
492 as zircon form broad clusters in three predominant orthogonal orientations (Fig. 5F).
493 This relationship is seen clearly in misorientation axis plots, where the >70º
494 misorientation axes coincide with {110} and (001) in the host zircon (Fig. 5F). The
495 granular reidite grains in the core have two main orientations that share a {110}
496 plane, which coincides with (001) of the host zircon (Fig. 5H). Dispersion of the data
497 is such that ~90 % of the data are within ±10º of this relationship (Fig. 5H). Low-
498 angle (<10º) misorientation axes are not systematically oriented, yet the >60º
499 misorientation axes form a single distinct cluster parallel with poles to (001) of the
500 host zircon (Fig. 5H).

Most of the rim yields good quality EBSD patterns and indexes well as zircon with relatively consistent single crystallographic orientation with some (<20º) systematic dispersion around poles to {112} (Fig. 5D, E). Several sets of bright lamellae cross-cut the rim and are visible in the BSE image; the thickest lamella indexes as reidite (Fig. 5B). The orientation relationship between reidite and the host zircon is such that one of the two $\{100\}_{zircon}$ is aligned with $\{112\}_{reidite}$, and another $\{112\}_{reidite}$ is aligned with respect to one of the $\{112\}_{zircon}$ (Fig. 5G).

3.2.3 Acraman zircon (impact melt rock)

The zircon from Acraman (grain 19) is ~40 μm across, polycrystalline, and comprised entirely of rounded, equant crystals of zircon with diameters ranging from 0.3 to 2.7 μm (Fig. 6A). In one part of the grain (core), the crystals impinge on one another, whereas some of the crystals around the rim are smaller than in the core and non-impinging (i.e., spatially isolated from one another). The interstitial material comprises a large Fe-Ti oxide grain and silicate glass, the latter having a composition that is indistinguishable from the surrounding impact melt (Fig. 6A). Therefore, the Fe-Ti oxide is interpreted to have crystallised within the impact melt after the formation of granular texture in the zircon. The CL response of zircon crystals is variable (Fig. 6B). Zircon crystals commonly contain one or more ~10 to ~70 nm diameter particles of ZrO_2 that are completely enclosed by zircon (Fig. 6A). However, the majority of these grains did not index with EBSD due to poor quality diffraction patterns. Misorientation analysis of polycrystalline zircon shows three distinct populations: (1) orientations that align closely (*i.e.*, within 30°) with the host grain (purple in Fig. 6C-D); (2) those at high-angles but with a systematic crystallographic relationship to the host grain (orange in Fig. 6C-D); and (3) those at high-angles but

with no systematic misorientation relationship to the host grain (*i.e.*, randomly orientated) (Fig. 6C, D). Low-angle (<30°) misorientation axes are common, but are not systematically oriented (Fig. 6E-F). Abundant high-angle misorientation axes have a systematic relationship with the host grain of 90° around <110>, and define the boundaries between three sub-domains within the impinging crystal domain (Fig. 6F).

4. Discussion

4.1 Establishing the microstructural processes of the case studies

4.1.1 Microstructures formed by dissociation at high T and low P (Mistastin Lake zircon)

The Mistastin Lake zircon does not contain twins, reidite, or granular texture, and there is no evidence that this grain has experienced high-pressure shock deformation. The morphology and orientation characteristics of the ZrO_2 grains are consistent with an interconnected, three-dimensional network of irregular tubules, that formed during dissociation of the host zircon. We interpret that the zircon reaction corona formed concentrically inwards from the original grain edge, producing ZrO_2 and liquid SiO_2. The minimum temperature required for dissociation (to tetragonal ZrO_2) is 1690 ºC at low pressures (1 GPa) (Figs 1B, 3B) (Butterman and Foster, 1967; Kaiser et al., 2008; Telle et al., 2015). The liquid silica dissociation product (that mixed with the surrounding impact melt everywhere away from the dissociation interface) is predicted to contain Zr (Fig. 1) (Telle et al., 2015), which is consistent with a halo of Zr enrichment in the surrounding glass (Fig. 2B) (Zanetti, 2015). However, both the concentration of dissolved Zr in the glass matrix and the exact polymorph of ZrO_2 are temperature-dependent, with cubic ZrO_2 stable above 2350 ºC (Kaiser et al., 2008). Nevertheless, growth of new zircon at the corona-core boundary (Fig. 4), could only

551 have occurred upon cooling below the zircon dissociation temperature (~1690 ºC),
552 partially consuming SiO_2 and ZrO_2, followed by reversion to baddeleyite upon
553 cooling below ~1200 ºC (Kaiser et al., 2008) (Figs 1 and 3). Orientation relationships
554 between zircon and ZrO_2-tet were not observed directly. A trace amount of ZrO_2-tet
555 was reported in the dissociation corona using Raman spectral mapping (Zanetti,
556 2015), but was not detected by EBSD because it is either too poorly crystalline to
557 index, it was located deeper below the surface than sampled by EBSD, or it was
558 removed during EBSD polishing.
559 The preservation of systematic orientation relationships among baddeleyite
560 grains suggest that the zirconia corona microstructure was achieved via solid-state
561 transformations. Orientation relationships among baddeleyite grains were used to
562 determine phase transformation heritage by one of two lineages: 1) zircon → ZrO_2-tet
563 → ZrO_2-mon (1690-2350 ºC), or 2) zircon → ZrO_2-tet → ZrO_2-cubic → ZrO_2-tet →
564 ZrO_2-mon (>2350 ºC). For each grain cluster in the corona, the twelve preserved
565 baddeleyite orientations (Fig. 4F) are best explained by a two-stage transformation
566 from an original ZrO_2-cubic grain (cf Cayron, 2007; Cayron et al., 2010; Humbert et
567 al., 2010) (Fig. 7). This means that the baddeleyite grain clusters are the products of
568 pre-existing cubic grains that had $\{100\}_{cubic}$ orientations aligned with $\{010\}_{baddeleyite}$
569 (Fig. 7). Furthermore, each of the three mutually-orthogonal orientation groups in
570 each cluster (*e.g.*, i-iii in Fig. 4F) is spatially distinct, defining pre-existing ZrO_2-tet
571 grains from the intermediate stage (cf Cayron, 2007; Cayron et al., 2010; Humbert et
572 al., 2010). The observed baddeleyite orientations for each corona cluster can only be
573 explained by twinning of ZrO_2-tet in three orientations, which formed during
574 transformation from ZrO_2-cubic (cf Kerschhofer et al., 2000; Cayron, 2007; Cayron et

575 al., 2010; Humbert et al., 2010). Therefore, the inferred phase heritage for the zirconia
576 corona can be traced back to ZrO_2-cubic.
577 The implications of these findings are three-fold: (1) Grain morphology and
578 crystallographic orientation of former ZrO_2 phases can be reconstructed; (2) the non-
579 systematic orientation relationships observed between zircon and its dissociation
580 products (in tis case, cubic ZrO_2) could be used as diagnostic criteria to infer the
581 former presence of zircon in other samples where zircon may have been completely
582 consumed/dissociated and only polycrystalline aggregates of zirconia remain; (3) the
583 analysis of orientation relationships to infer the former presence of phases with
584 known stabilities constitutes a novel approach to thermobarometry. All textural and
585 orientation evidence indicate that the Mistastin Lake grain experienced an extreme
586 thermal excursion that did not fully dissociate prior to quenching of the host rock to
587 glass, and also that the initial zircon was not shock metamorphosed prior to
588 incorporation into the impact melt (Figs 1, 3).
589
590 ***4.1.2 Microstructures formed by reidite transformation and reversion (Ries crater***
591 ***$ZrSiO_4$)***
592 The Ries zircon grain contains two types of reidite; lamellar reidite
593 preferentially formed in the crystalline rim domain, and granular reidite formed
594 chiefly in the partially metamict core domain (Fig. 5). This observation suggests that
595 intrinsic properties of each domain influenced the reidite transformation mechanism.
596 The spatial restriction of lamellar reidite to non-metamict domains in zircon has been
597 observed elsewhere (Cavosie et al., 2015a; Reddy et al., 2015; Erickson et al., in
598 press). The reasons for this are twofold: First, reduction of the elastic moduli that
599 accompanies radiation damage means that metamict domains are more compliant and

600 achieve comparatively lower stresses as shock waves pass through the grain (Timms
601 et al., in review). Second, defects that result from radiation damage are obstacles for
602 lamellae propagation (Timms et al., in review). Higher defect densities associated
603 with metamictisation at the time of impact could have provided both suitable
604 nucleation sites and sufficient strain energy to overcome the nucleation energy barrier
605 for granular reidite formation (Erickson et al., in press).
606 The observed crystallographic orientation relationships between the host
607 zircon and both granular and lamellar reidite varieties are consistent with the findings
608 of other studies (Leroux et al., 1999; Cavosie et al., 2015a; Reddy et al., 2015;
609 Erickson et al., in press). The two dominant, approximately orthogonal reidite
610 orientations with a coincident <110> and a single high-angle (~90º) misorientation
611 axis coincident with <001> of the host zircon are consistent with epitaxial nucleation
612 of reidite granules via more than one of the eight symmetrically equivalent
613 transformation variants (Fig. 5h, 7) (Erickson et al., in press).
614 The formation of granular zircon with systematic ~90º misorientations, *i.e.*,
615 <110> of the neoblasts is aligned with [001] of the host grain, in the core domain of
616 the Ries zircon is inconsistent with subgrain rotation recrystallization, which is
617 expected to yield low-angle misorientations. However, the reversion of reidite back to
618 zircon can occur with one of two main, symmetrically equivalent disorientation
619 relationships, such that either of the conjugate $\{110\}_{reidite} = (001)_{zircon}$ (Fig. 8).
620 Therefore, the transformation sequence zircon→reidite→zircon can result in up to
621 three approximately orthogonal orientations of neoformed zircon from one initial
622 zircon orientation (Fig. 8). If each orientation permutation is equally likely to form
623 during each of the transformation steps, then the original zircon orientation dominates
624 the final microstructure (Fig. 8). Hence, the orientation relationships between granular

625 zircon and host can be explained if the zircon neoblasts transformed from reidite (Fig.
626 8).
627 The development of neoformed zircon granules (neoblasts) by reversion from
628 reidite has two significant implications: (1) zircon neoblast growth necessarily post-
629 dated reidite transformation, and most likely occurred during decompression when the
630 grain returned to the zircon stability field (Fig. 1a); and (2) a systematic orthogonal
631 disorientation relationship (~90° around <110>) between zircon granules can be used
632 as an indicator of zircon reversion from reidite (Fig. 8). This interpretation has been
633 used to explain similar orientation relationships between neoblasts and to infer the
634 former presence of reidite in granular zircon from Meteor Crater (Cavosie et al.,
635 2016b).
636 The presence of lamellar reidite indicates that the grain from the Ries crater must
637 have experienced shock pressures >30 GPa (Fig. 3). Furthermore, if a shear
638 mechanism is not required for the formation of granular reidite (Cavosie et al.,
639 2015a), then this form of reidite could have nucleated at lower, hydrostatic conditions
640 (>12 GPa), and potentially formed before the lamellar reidite during the same event
641 (Figs 3, 9). However, this grain does not preserve evidence for dissociation, and so
642 the maximum temperature during decompression and zircon neoblast growth cannot
643 have exceeded 1690 ºC (Fig. 3, 9).
644
645 ***4.1.3 Microstructures formed at high P and high T (Acraman zircon)***
646 Zircon neoblasts are pervasive in the Acraman zircon grain. As outlined above, the
647 presence of ~90º / <110> disorientation between impinging neoblasts in the lower part
648 of the Acraman zircon is consistent with nucleation of new grains by reversion from
649 reidite (e.g., Cavosie et al., 2016b). However, the presence of baddeleyite indicates

650 that dissociation must have occurred, at least locally. The misorientation relationship
651 is inconsistent with those predicted from solid state reversion from ZrO_2 after
652 dissociation, which could generate a variety of 90º disorientation relationships among
653 neoblasts, but would not produce specific systematic disorientations of 90º / <110>
654 (Fig. 4, 7). Therefore, it is interpreted that the Acraman zircon grain experienced P-T
655 conditions where reidite was stable.
656 The baddeleyite crystals are fully enclosed in zircon neoblasts, which suggests that
657 growth of zircon neoblasts occurred after dissociation, partially consuming ZrO_2 and
658 sourcing SiO_2 from the surrounding impact melt. Therefore, the zircon specimen must
659 have experienced post-decompression temperatures of >1690 ºC (Fig. 3B). The
660 random (non-systematic) orientations of the peripheral, isolated zircon neoblasts
661 indicates that their orientations are not inherited from the original zircon grain. The
662 absence of any crystallographic inheritance from the original host grain requires an
663 alternative explanation than where epitaxy is prevalent. It is difficult to determine
664 whether or not the non-systematically oriented neoblasts formed via solid state
665 transformation from zircon, reidite, or ZrO_2 phases and were physically dispersed and
666 non-systematically rotated within the silicate melt, or crystallised directly from melt.
667 However, it seems unlikely that a fluid (either Zr-saturated melt or an immiscible
668 ZrO_2 liquid) generated from a decomposed zircon would have remained coherent long
669 enough to recrystallize as ZrO_2 and zircon because the viscosities of melt phases at
670 this temperature must have been extremely low, and they would have been susceptible
671 to diffusive and turbulent mixing during excavation and crater modification.
672 Furthermore, a dynamic melt environment would have physically dispersed granules
673 more heterogeneously than is observed. Perhaps the best explanation is that these
674 granules nucleated initially in random orientations. Nevertheless, it is clear that

675 granular texture formation was relatively late in the pressure-temperature history of
676 the Acraman impact melt, and only occurred after zircon stabilized upon cooling
677 below 1690 ºC (Fig. 3B) (Butterman and Foster, 1967; Kaiser et al., 2008)
678
679 ***4.2 Application of the phase diagram and orientation relationships to infer P-T***
680 ***paths***
681 Inevitably, the exact shape and size of P-T trajectories during impact events will vary
682 within and among impact structures, and will depend on the size, velocity, and
683 composition of the impactor, the position of the target rock relative to the initial
684 impact site, and the intrinsic material properties of the target rock (*e.g.*,
685 sedimentary/porous vs. crystalline/dense; permeable vs. impermeable), meso-scale
686 heterogeneity of shock heating and compression, and the rate of cooling of the
687 impactites that host the shocked zircon at high temperatures.
688 The three zircon samples in this study preserve microstructures that indicate
689 different pressure-temperature paths at extreme conditions (Fig. 3, 9). These case
690 studies illustrate how shock conditions can be inferred and used to characterise
691 different trajectories in pressure-temperature space (Fig. 9). It also shows,
692 conceptually, how these trajectories make testable predictions about the potential for
693 preservation or overprinting of early-formed microstructures and shock-induced
694 phases. The zircon grain from the lithic clast in the Ries suevite (*i.e.*, near the top of
695 impactite deposits, typically characterized by relatively fast cooling rates)
696 experienced a P-T loop that involves moderate shock pressure and heating (shown by
697 the red line in Fig. 9). The Ries zircon was seemingly "protected" from direct contact
698 with any impact melt (in this case *flädle*) by its own surrounding host rock clast,
699 which was subjected to stage II shock metamorphism, and so experienced post-shock

700 cooling rates that were high enough to inhibit the complete reversion of reidite to
701 zircon.
702 In contrast, the zircon in the Mistastin Lake impact melt (either a terrace melt
703 pond or a more typical melt sheet overlying the crater basement and basal breccias,
704 and likely originally overlain by some suevitic impactites) may simply represent a
705 weakly shocked (or unshocked) target rock-derived grain that was entrained by the
706 hot, fluid melt. This grain essentially underwent an extreme temperature excursion at
707 very low-pressure (blue line of Fig. 9). Onorato et al. (1978) constrain the initial
708 cooling of impact melt sheets to within ~100 seconds, and so the cooling rate of the
709 Mistastin lake zircon was likely higher than that experienced by the Ries grain.
710 The Acraman grain is inferred to have undergone a P-T loop where post-shock
711 decompression temperatures were high enough for dissociation of zircon (green line
712 of Fig. 8). Given that a post-shock temperature of 1500 ºC has been estimated for
713 non-porous quartzo-feldspathic rocks shocked to 60 GPa (Stöffler, 1971), it is
714 therefore likely that the Acraman zircon experienced shock pressures >60 GPa. The
715 Acraman melt rock occurs very close to "ground zero", and formed by deeper melt
716 injection into the uplifted crater basement inside the central uplift, presumably
717 beneath the melt sheet. Subsequent "stage I" high-T cooling of the hot melt and wall
718 rock was relatively slow, permitting growth of Fe-Ti oxides and spinifex albite. All of
719 the P-T paths are consistent with granular textures forming late in the P-T history of
720 shocked zircon. Granular zircon can form from the reversion of reidite to zircon by
721 heating above 1200 ºC (Cavosie et al., 2016b), or the annealing of dissociated zircon,
722 where ZrO_2 grains react with Si-saturated impact melt to reconstitute zircon
723 (Wittmann et al., 2006; Wittmann et al., 2009).

724 The new phase diagram also helps to relate microstructure to conditions
725 experienced by zircon reported from other impact structures, such as Vredefort in
726 South Africa (Fig. 9A, B, C, line (i)) (Moser et al., 2009; Cavosie et al., 2010; Moser
727 et al., 2011; Erickson et al., 2013a; Cavosie et al., 2015b; Montalvo et al., in press),
728 Sudbury in Ontario, Canada (Fig. 9A, B, C, line (i)) (Thomson et al., 2014), Rock
729 Elm in Wisconsin, USA (Fig. 9A-D) (Cavosie et al., 2015a), the Araguainha impact
730 structure of Brazil (Tohver et al., 2012), the impact crater that produced the Stac Fada
731 Member in Scotland (Fig. 9B, D) (Reddy et al., 2015; Reddy et al., 2016), Meteor
732 Crater in Arizona, USA (Fig. 9F) (Cavosie et al., 2016b), Chicxulub in Mexico (Fig.
733 9I) (Wittmann et al., 2006), and impact craters on the Moon (Fig. 9A, B, C, lines (i)
734 and (ii)) (Timms et al., 2012b).
735
736 ***4.3 Determining phase heritage: A new approach for extreme thermobarometry***
737 This study demonstrates that zircon grains can undergo a variety of structural and
738 phase changes during impact events, which depend on the P-T trajectory. Here we
739 identify two different approaches to 'extreme thermobarometry' using microstructures
740 of zircon and the new P-T phase diagram. The first approach involves linking 'direct
741 evidence' to the phase diagram. This includes identification of preserved high-P
742 phases such as reidite (~30 GPa), diagnostic shock deformation microstructures such
743 as twins in zircon (~20 GPa), and/or low-P, high-T processes, such as dissociation of
744 zircon to zirconia and silica (~1687 ºC).
745 The second approach involves gaining insight into P-T conditions from
746 crystallographic orientation relationships to infer the former presence of phases that
747 are no longer present. This approach includes orientation relationships between
748 neoformed zircon granules to reveal the crystallographic legacy of former twins

749 (tentatively ≥20 GPa shock conditions), reversion from reidite (indicating ≥30 GPa
750 for shock metamorphism), and orientation relationships between ZrO_2 produced by
751 zircon dissociation to reveal the former presence of cubic zirconia (≥2370 ºC) or
752 tetragonal zirconia (≥ ~1200 ºC). In this way, orientation analysis can be used to
753 identify the former presence of phases, and even elucidate the possible sequence of
754 transformations: a concept we refer to here as 'phase heritage'. This approach cannot
755 be applied to situations where orientation relationships with the original host have
756 been lost; such as if the P-T history involves a stage where ZrO_2 was liquid (*i.e.*, total
757 fusion), or when physical rotation of solid grains in a melt has occurred. The phase
758 heritage approach outlined in this paper is particularly useful where other evidence of
759 earlier processes has been erased, such as in granular shocked zircon.
760 Currently, there are few published studies that quantify microstructures of
761 zircon that have experienced extreme conditions, and so there is merit in collecting
762 more data from natural samples from different environments. The case studies
763 highlighted here focus on impact processes. However, our approach is equally
764 applicable to zircon sourced from (or having travelled through) the mantle, or, for
765 example, zircon in fulgurites, that have been modified by lightning strike. The phase
766 diagram could have implications for recycling of crustal zircon and zirconia through
767 the Earth's mantle, kimberlite zircon, and consequently global behavior of Zr.
768
769 **Conclusions**
770 • The new P-T diagram constructed from available published data provides
771 first-order constraints of the stability of $ZrSiO_4$ (zircon, reidite), ZrO_2
772 (including baddeleyite) and SiO_2 polymorphs. Up-pressure extrapolation of
773 the dissociation reaction line (zircon → ZrO_2 + SiO_2) has been calculated to

774 have a Clapeyron slope of 2.9 x10^{-3} GPa / °C, and so for a zero-pressure
775 intercept of 1690 ºC, this reaction intersects the cristobalite solidus at ~0.14
776 GPa.
777 • Dissociation of zircon is a high-T, low-P process, that can occur via thermal
778 processes alone (*e.g.*, entrainment into an impact melt) or during to after shock
779 decompression. Dissociation can result in numerous, non-systematic cubic
780 ZrO_2 orientations with respect to the original zircon. Upon cooling, each cubic
781 grain transforms to up to twelve unique baddeleyite orientation variants (via
782 an intermediate stage of up to three tetragonal ZrO_2 variants), which permits
783 the phase heritage to be inferred, providing constraints on post-shock
784 temperature history of the sample.
785 • Shock compression results in the transformation of zircon to lamellar or
786 granular reidite, which produces up to eight unique crystallographic
787 orientation variants with $(001)_{zircon} = \{110\}_{reidite}$ that can be assigned to two
788 groups that are broadly orthogonally aligned: In each group, reidite (001) are
789 within 10º of each other.
790 • Reversion of reidite back to zircon by the reverse orientation relationship or its
791 symmetric equivalents produces up to three broadly orthogonal orientations,
792 including the original zircon orientation plus two where (001) of the new
793 zircon is aligned with {110} of the original orientation. This results in a
794 characteristic ~90º / {110} disorientation between orientation domains in
795 neoformed zircon that can be used as indirect evidence of the former presence
796 of reidite.
797 • In impact settings, granular zircon texture forms during or after shock
798 decompression at high-T where zircon is stable, and preferentially forms in

799 domains that contain defects (*e.g.*, metamict domains, lamellae interfaces,
800 etc.), where the energy barrier for nucleation is lower.
801 • Combining microstructural analysis of zircon with new P-T diagrams for
802 $ZrSiO_4$-ZrO_2-SiO_2 is a useful approach to identify P-T paths during impact
803 events.
804
805 **Acknowledgements**
806 M. Zanetti acknowledges support from a Barringer Family Award for Impact
807 Cratering Research, the Mineralogical Society of America Grant for Student Research
808 in Mineralogy and Petrology, and the Eugene M. Shoemaker Award for Impact Crater
809 Research, and a Meteoritical Society Travel Grant (NASA Cosmochemistry
810 Program). A. Cavosie acknowledges support from the National Science Foundation
811 (EAR-1145118), the NASA Astrobiology program, and a Curtin Research
812 Fellowship. T. Erickson acknowledges a Curtin International Postgraduate
813 Scholarship. E. Tohver acknowledges support from the Australian Research Council
814 (DP0988190). Thorsten Geisler and ZERIN (Centre for Ries Crater and Impact
815 Research in Nördlingen) are thanked for the acquisition of the sample from the Ries
816 crater. We thank Sandy Morris, Yardea Station, for his kind support and granting E.
817 Tohver and M. Schmieder access to the Acraman impact structure on his private land.
818 We acknowledge technical support from the Microscopy and Microanalysis Facility
819 at Curtin. Two anonymous reviewers are acknowledged for their constructive reviews
820 of the manuscript, and A. Gomez-Tuena is thanked for editorial handling.
821
822 **Figure Captions**

823 Figure 1. A. Pressure-temperature-composition (P-T-X) space for the ZrO_2-$ZrSiO_4$-
824 SiO_2 system, showing the scope of previous compilations and the relative positions of
825 the figures presented in this study. Stish = stishovite; Coes = coesite; Tridy =
826 tridymite; Qtz = quartz; Zrn = zircon; Bdy = baddeleyite; liq = liquid; oI and oII =
827 orthorhombic; t = tetragonal; c = cubic. B. T-X phase diagram for ZrO_2-$ZrSiO_4$-SiO_2
828 system modified after Telle et al. (2015). Tridymite stability after Swamy et al.
829 (1994). Dashed line represents zircon dissociation reaction after Curtis and Sowman
830 (1953).
831
832 Figure 2. Images showing rock textures of the case study samples. A. Optical
833 photomicrograph of impact glass from the Mistastin Lake impact structure. Particles
834 are partially digested minerals and lithic clasts. Plane polarised light. B. Backscattered
835 electron (BSE) image of the zircon used in this study (white particle) within the
836 Mistastin Lake impact glass. Pale grey halo and trail is silicate glass that is enriched
837 in Zr (by up to 1 wt. %). C. Optical photomicrograph of zircon-bearing clast in
838 suevite from the Ries impact structure that predominantly consists of maskelynite and
839 amorphous SiO_2. The zircon used in this study is central in the image, surrounded by
840 a dark rectangle of electron beam damaged matrix phases. Plane polarised light. D.
841 Optical photomicrograph of impact melt rock from the Acraman impact structure.
842 Spinifex textured albite is commonly radial around partially digested mineral and
843 lithic clasts.
844
845 Figure 3. Pressure-temperature diagrams illustrating available data for conditions of
846 $ZrSiO_4$ transformations and dissociation to ZrO_2 and SiO_2. A. (i) $ZrSiO_4$ polymorphs
847 (zircon and reidite). Field labelled ‘crust’ represents metamorphic P-T conditions

848 experienced by the Earth's crust, and includes ultra-high pressure and ultra-high
849 temperature metamorphism. (ii) expanded P-T field showing other constraints from
850 shock experiments. Arrows show examples of trajectories of different materials from
851 shock experiments. Porous sandstone = Kieffer et al. (1976); Quartz = Wackerle
852 (1962); Olivine = Holland and Ahrens (1997). B. (i) Stability fields for zircon
853 dissociation products SiO_2 (thin lines coloured fields) and ZrO_2 polymorphs (thicker
854 lines and annotated fields). (ii) Expanded P-T field showing zircon dissociation
855 reaction line (see text for calculation and discussion). Stish = stishovite; Coes =
856 coesite; Tridy = tridymite; Cristob = cristobalite; Qtz = quartz; bdy = baddeleyite; liq
857 = liquid; oI and oII = orthorhombic; t = tetragonal; c = cubic. (1) Marqués et al.
858 (2006) and Du et al. (2012); (2) Reid and Ringwood (1969); (3) Liu (1979); (4) van
859 Westrenen et al. (2004); (5) Knittle and Williams (1993); (6) Leroux et al. (1999); (7)
860 Kusaba et al. (1985); (8) Morozova (2015); (9) Ono et al. (2004a); (10) Chaplot et al.
861 (2006); (11) Tange and Takahashi (2004); (12) Butterman and Foster (1967), Kaiser
862 et al. (2008); (13) Curtis and Sowman (1953); (14) Dutta and Mandal (2012); Silica
863 phase transition univariant lines after Swamy et al. (1994) and references therein;
864 Zirconia polymorph transition univariant lines after Bouvier et al. (2000) and
865 references therein; (15) Ohtaka et al. (1994); (16) Arashi et al. (1990).
866
867 Table 1. Thermodynamic parameters used to calculate zircon dissociation reaction
868 line. Temperature in °K. Data source references indicated by superscript letters: a =
869 O'Neill (2006); b = Bouvier et al. (2002); c = Robie and Hemingway (1995); d = Ortiz
870 et al. (2007); e = Mao et al. (2001); f = Adams et al. (1985); g = Mittal et al. (1998); h
871 = Subbarao et al. (1974).
872

873 Table 2. Scanning electron microscopy settings and electron backscatter diffraction
874 analysis acquisition and processing parameters. (Böhm, 1925; Teufer, 1962; Sands,
875 1969; Hazen and Finger, 1979; Kirfe et al., 1979; Downs and Palmer, 1994; Hill and
876 Cranswick, 1994; Bondars et al., 1995; Farnan et al., 2003).
877
878 Figure 4. Mistastin Lake zircon in holohyaline impact glass. A. Cathodoluminescence
879 image. Sector zoned igneous core surrounded by a bright, narrow, intermediate zircon
880 domain and dark baddeleyite + silicate glass rim. B. Backscattered electron image of
881 inset shown in A. C. Detail of backscattered electron image from inset shown in B. D.
882 Orientation map from electron backscatter diffraction data. Zircon coloured for
883 disorientation from a reference orientation shown by red cross near the center of
884 grain. Baddeleyite assigned inverse pole figure (IPF) colour scheme. Special
885 orientation boundaries in baddeleyite are shown as coloured lines. E. Detail of EBSD
886 map from inset shown in D. Pole figures for selected baddeleyite grain clusters
887 (numbered in E) plotted in the reference frame of the remaining zircon (refer to grey
888 symbols on upper left plot). Sub-domains within each grain cluster are oriented
889 orthogonally to one another (*e.g.*, i, ii and iii in cluster 3). Pole figures are equal area,
890 lower hemisphere plots in the EBSD map x-y-z reference frame.
891
892 Figure 5. Ries Crater zircon. A. CL image showing bright rim with planar features
893 (*e.g.*, white arrow) and patchy yet dark core. B. BSE image showing inverse contrast
894 relationship to CL image. Bright linear features can be seen in the rim (i). C. Phase
895 map from EBSD data showing zircon-dominated rim domain (i) and core domain (ii)
896 with zircon and reidite. D. Orientation map from EBSD data. Zircon and reidite
897 assigned IPF colour scheme. Indexed reidite lamellae shown in domain (iii). E-H.

898 Pole figures (top row) and equal area projections of disorientation axes binned by
899 disorientation angle (bottom row) for host zircon in domain (i), and zircon and reidite
900 in domains (ii) and (iii), respectively. Disorientation axis plots with >300 points have
901 been contoured (max values are multiples of mean uniform distribution). Pole figures
902 are equal area, lower hemisphere plots in the EBSD map x-y-z reference frame.
903
904 Figure 6. Acraman zircon. A. BSE image. Bdy = baddeleyite. B. CL image. C.
905 Orientation map from EBSD data. Zircon assigned IPF colour scheme. D. Pole figures
906 for zircon. Colour scheme as in C. F. Equal area projections of disorientation axes
907 binned by disorientation angle. Pole figures are equal area, lower hemisphere plots in
908 the EBSD map x-y-z reference frame.
909
910 Figure 7. Schematic diagram to show possible crystallographic orientation
911 relationships associated with dissociation of a single zircon to ZrO_2, followed by
912 several polymorphic ZrO_2 phase transformations determined from the Mistastin Lake
913 grain. Each cubic ZrO_2 variant can result in three tetragonal ZrO_2 orientations, which
914 in turn can lead to up to twelve distinct orientation variants of baddeleyite. Grey box
915 shows an example orientation lineage across multiple phase transformations. See text
916 for further discussion.
917
918 Figure 8. Schematic diagram to show the possible crystallographic orientation
919 relationships of transformation from a single zircon to reidite followed by reversion to
920 zircon using known relationships (Leroux et al., 1999; Cavosie et al., 2015a; Erickson
921 et al., in press). Pole figures summarise the key relationships.
922

Figure 9. Schematic diagram to summarise different types of microstructure that can form during impact events, and how they link to pressure-temperature conditions for several example P-T paths (red, green and blue lines). Zrn = zircon; Reid = reidite. Stability fields based on Fig. 2. See text for discussion.

Appendix 1

The slope of a reaction in pressure-temperature space (Clapeyron slope) given by the change in entropy with respect to molar volume such that:

$$dPdT = \Delta S \Delta V$$

Therefore if it is possible to calculate the changes in entropy and molar volume for a reaction, in this case zircon → ZrO_2-tet + SiO_2-crist, then the slope of this reaction may be determined.

The temperature dependence of the entropy and molar volume can be approximated using expressions for the heat capacity and thermal expansion, respectively, of each phase in the reaction:

$$ST,1 = STref,1 + \int_{Tref}^{T} CpTdT$$

$$VT,1 = V0ea0T - Tref$$

Where Tref is the reference temperature for S and V_0

947

948 Similar expressions exist for extrapolations to higher pressure but the parameters in
949 Table 1 for the phases of interest give a steep slope (29°C/bar) that intersects the
950 silica solidus (~1715°C) at 1.4 kbar.

951

952 **References**

953

954 Adams, J.W., Nakamura, H.H., Ingel, R.P. and Rice, R.W., 1985. Thermal expansion
955 behavior of single-crystal zirconia. Journal of the American Ceramic Society,
956 68: C-228-C-231.
957 Allen, G.C., Simpson, C.J., McPhie, J. and Daly, S.J., 2003. Stratigraphy, distribution
958 and geochemistry of widespread felsic volcanic units in the Mesoproterozoic
959 Gawler Range Volcanics, South Australia*. Australian Journal of Earth
960 Sciences, 50: 97-112.
961 Allen, S.R., McPhie, J., Ferris, G. and Simpson, C., 2008. Evolution and architecture
962 of a large felsic Igneous Province in western Laurentia: The 1.6 Ga Gawler
963 Range Volcanics, South Australia. Journal of Volcanology and Geothermal
964 Research, 172(1-2): 132-147.
965 Arashi, H., Yagi, T., Akimoto, S. and Kudoh, Y., 1990. New high-pressure phase of
966 ZrO_2 above 35 GPa. Physical Review B, 41(7): 4309.
967 Ayers, J.C., Zhang, L., Luo, Y. and Peters, T.J., 2012. Zircon solubility in alkaline
968 aqueous fluids at upper crustal conditions. Geochimica et Cosmochimica Acta,
969 96: 18-28.
970 Bansal, G.K. and Heuer, A.H., 1972. On a martensitic phase transformation in
971 zirconia (ZrO_2) - metallographic evidence. Acta Metallurgica, 20: 1281-1289.

Bauberger, W., Mielke, H., Schmeer, D. and Stettner, G., 1974. Petrographische Profildarstellung der Forschungsbohrung Nördlingen 1973. Geologica Bavarica, 72: 33-34.

Bellucci, J.J., Whitehouse, M.J., Nemchin, A.A., Snape, J.F., Pidgeon, R.T., Grange, M., Reddy, S.M. and Timms, N., 2016. A scanning ion imaging investigation into the micron-scale U-Pb systematics in a complex lunar zircon. Chemical Geology, 438: 112-122.

Bernini, D., Audétat, A., Dolejš, D. and Keppler, H., 2013. Zircon solubility in aqueous fluids at high temperatures and pressures. Geochimica et Cosmochimica Acta, 119: 178-187.

Block, S., Jornada, J.D. and Piermarini, G.J., 1985. Pressure‐Temperature Phase Diagram of Zirconia. Journal of the American Ceramic Society, 68(9): 497-499.

Boehnke, P., Watson, E.B., Trail, D., Harrison, T.M. and Schmitt, A.K., 2013. Zircon saturation re-revisited. Chemical Geology, 351: 324-334.

Bohlen, S.R. and Boettcher, A.L., 1982. The quartz⇆ coesite transformation: a precise determination and the effects of other components. Journal of Geophysical Research: Solid Earth, 87(B8): 7073-7078.

Böhm, J., 1925. Über das Verglimmen einiger Metalloxyde. Z. Anorg. Allg. Chem., 149: 217-222.

Bohor, B.F., Betterton, W.J. and Krogh, T.E., 1993. Impact-shocked zircons: discovery of shock-induced textures reflecting increasing degrees of shock metamorphism. Earth and Planetary Science Letters, 119(3): 419-424.

995 Bondars, B., Heidemane, G., Grabis, J., Laschke, K., Boysen, H., Schneider, J. and
996 Frey, F., 1995. Powder diffraction investigations of plasma sprayed zirconia.
997 Journal of Materials Science, 30(6): 1621-1625.
998 Boullier, A.M., 1980. A preliminary study on the behaviour of brittle minerals in a
999 ductile matrix: example of zircons and feldspars. Journal of Structural
1000 Geology, 2(1): 211-217.
1001 Bouvier, P., Djurado, E., Lucazeau, G. and Le Bihan, T., 2000. High-pressure
1002 structural evolution of undoped tetragonal nanocrystalline zirconia. Physical
1003 Review B, 62(13): 8731-8737.
1004 Bouvier, P., Godlewski, J. and Lucazeau, G., 2002. A Raman study of the
1005 nanocrystallite size effect on the pressure–temperature phase diagram of
1006 zirconia grown by zirconium-based alloys oxidation. Journal of Nuclear
1007 Materials, 300(2): 118-126.
1008 Butterman, W.C. and Foster, W.R., 1967. Structure of gel derived and quenched
1009 glasses in the Al_2O_3-ZrO_2-SiO_2 system. American Mineralogist: 52-884.
1010 Cavosie, A.J., Erickson, T.M. and Timms, N.E., 2015a. Nanoscale records of ancient
1011 shock deformation: Reidite ($ZrSiO_4$) in sandstone at the Ordovician Rock Elm
1012 impact crater. Geology, 43(4): 315-318.
1013 Cavosie, A.J., Erickson, T.M., Timms, N.E., Reddy, S.M., Talavera, C., Montalvo,
1014 S.D., Pincus, M.R., Gibbon, R.J. and Moser, D., 2015b. A terrestrial
1015 perspective on using ex situ shocked zircons to date lunar impacts. Geology,
1016 43(11): 999-1002.
1017 Cavosie, A.J., Montalvo, P.E., Timms, N.E. and Reddy, S.M., 2016a. Nanoscale
1018 deformation twinning in xenotime, a new shocked mineral, from the Santa Fe
1019 impact structure (New Mexico, USA). Geology, 44(10): 803-806.

1020 Cavosie, A.J., Quintero, R.R., Radovan, H.A. and Moser, D.E., 2010. A record of
1021 ancient cataclysm in modern sand: Shock microstructures in detrital minerals
1022 from the Vaal River, Vredefort Dome, South Africa. Geological Society of
1023 America Bulletin, 122(11-12): 1968-1980.
1024 Cavosie, A.J., Timms, N.E., Erickson, T.M., Hagerty, J.M. and Hörz, F., 2016b.
1025 Transformations to granular zircon revealed: Twinning, reidite, and ZrO_2 in
1026 shocked zircon from Meteor Crater. Geology, 44(9): 703-706.
1027 Cavosie, A.J., Timms, N.E. and Farthing, D., 2016c. Insights into impact melt
1028 conditions from dissociated zircon in medieval tin slag. Geological Society of
1029 America Abstracts with Programs, 48(7): 290-16.
1030 Cayron, C., 2007. ARPGE: a computer program to automatically reconstruct the
1031 parent grains from electron backscatter diffraction data. J Appl Crystallogr,
1032 40(Pt 6): 1183-1188.
1033 Cayron, C., Douillard, T., Sibil, A., Fantozzi, G. and Sao-Jao, S., 2010.
1034 Reconstruction of the Cubic and Tetragonal Parent Grains from Electron
1035 Backscatter Diffraction Maps of Monoclinic Zirconia. Journal of the
1036 American Ceramic Society, 93(9): 2541-2544.
1037 Chaplot, S.L., Pintschovius, L. and Mittal, R., 2006. Phonon dispersion relation
1038 measurements on zircon, ZrSiO4. Physica B: Condensed Matter, 385-386:
1039 150-152.
1040 Chevalier, J., Gremillard, L., Virkar, A.V. and Clarke, D.R., 2009. The Tetragonal-
1041 Monoclinic Transformation in Zirconia: Lessons Learned and Future Trends.
1042 Journal of the American Ceramic Society, 92(9): 1901-1920.
1043 Christian, J.W. and Mahajan, S., 1995. Deformation Twinning. Progress in Materials
1044 Science, 39: 1-57.

1045 Clark, C., Healy, D., Johnson, T., Collins, A.S., Taylor, R.J., Santosh, M. and Timms,
1046 N.E., 2015. Hot orogens and supercontinent amalgamation: A Gondwanan
1047 example from southern India. Gondwana Research, 28(4): 1310-1328.
1048 Cohen, L.H. and Klement, W., 1967. High-low quartz inversion: Determination to 35
1049 kilobars. Journal of Geophysical Research, 72(16): 4245–4251.
1050 Corfu, F., Hanchar, J.M., Hoskin, P.W. and Kinny, P., 2003. Atlas of zircon textures.
1051 Reviews in Mineralogy and Geochemistry, 53(1): 469-500.
1052 Crow, C.A., Jacobsen, B., McKeegan, K.D. and Moser, D.E., 2015. Investigating
1053 zircon shock microstructures with NanoSIMS, Lunar and Planetary Science
1054 Conference. Lunar and Planetary Science Institute, Woodlands, Texas, pp.
1055 2470.
1056 Curtis, C.E. and Sowman, H.G., 1953. Investigation of the thermal dissociation,
1057 reassociation, and synthesis of zircon. Journal of the American Ceramic
1058 Society, 36(6): 190-198.
1059 Deloule, E., Chaussidon, M., Glass, B.P. and Koeberl, C., 2001. U–Pb isotopic study
1060 of relict zircon inclusions recovered from Muong Nong-type tektites.
1061 Geochimica et Cosmochimica Acta, 65(11): 1833-1838.
1062 Deutsch, A., & Schärer, U., 1990. Isotope systematics and shock-wave
1063 metamorphism: II. U-Pb and Rb-Sr in naturally shocked rocks; the Haughton
1064 Impact Structure, Canada. Geochimica et Cosmochimica Acta, 54(12): 3435-
1065 3447.
1066 Deutsch, A. and Schärer, U., 1990. Isotope systematics and shock-wave
1067 metamorphism: I. U-Pb in zircon, titanite and monazite, shocked
1068 experimentally up to 59 GPa. Geochimica et Cosmochimica Acta, 54(12):
1069 3427-3434.

1070 Di Toro, G. and Pennacchioni, G., 2004. Superheated friction-induced melts in zoned
1071 pseudotachylytes within the Adamello tonalites (Italian Southern Alps).
1072 Journal of Structural Geology, 26(10): 1783-1801.
1073 Di Vincenzo, G. and Skála, R., 2009. ^{40}Ar–^{39}Ar laser dating of tektites from the Cheb
1074 Basin (Czech Republic): Evidence for coevality with moldavites and influence
1075 of the dating standard on the age of the Ries impact. Geochimica et
1076 Cosmochimica Acta, 73(2): 493-513.
1077 Downs, R.T. and Palmer, D.C., 1994. The pressure behavior of c~-cristobalite.
1078 American Mineralogist, 79: 9-14.
1079 Du, J., Devanathan, R., René Corrales, L. and Weber, W.J., 2012. First-principles
1080 calculations of the electronic structure, phase transition and properties of
1081 $ZrSiO_4$ polymorphs. Computational and Theoretical Chemistry, 987: 62-70.
1082 Dutta, R. and Mandal, N., 2012. Structure, elasticity and stability of reidite ($ZrSiO_4$)
1083 under hydrostatic pressure: A density functional study. Materials Chemistry
1084 and Physics, 135(2-3): 322-329.
1085 El Goresy, A., 1965. Baddeleyite and its significance in impact glasses. Journal of
1086 Geophysical Research, 70(14): 3453-3456.
1087 El Goresy, A., Dubrovinsky, L., Sharp, T.G. and Chen, M., 2004. Stishovite and post-
1088 stishovite polymorphs of silica in the shergotty meteorite: their nature,
1089 petrographic settings versus theoretical predictions and relevance to Earth's
1090 mantle. Journal of Physics and Chemistry of Solids, 65(8): 1697-1608.
1091 Erickson, T.M., Cavosie, A.J., Moser, D.E., Barker, I.R. and Radovan, H.A., 2013a.
1092 Correlating planar microstructures in shocked zircon from the Vredefort Dome
1093 at multiple scales: Crystallographic modeling, external and internal imaging,
1094 and EBSD structural analysis. American Mineralogist, 98(1): 53-65.

1095 Erickson, T.M., Cavosie, A.J., Moser, D.E., Barker, I.R., Radovan, H.A. and Wooden,
1096 J., 2013b. Identification and provenance determination of distally transported,
1097 Vredefort-derived shocked minerals in the Vaal River, South Africa using
1098 SEM and SHRIMP-RG techniques. Geochimica et Cosmochimica Acta, 107:
1099 170-188.
1100 Erickson, T.M., Cavosie, A.J., Pearce, M.A., Timms, N.E. and Reddy, S.M., 2016.
1101 Empirical constraints on shock features in monazite using shocked zircon
1102 inclusions. Geology, 44(8): 635-638.
1103 Erickson, T.M., Pearce, M.A., Reddy, S.M., Timms, N.E., Cavosie, A.J., Bourdet, J.,
1104 Rickard, W.D.A. and Nemchin, A.A., in press. Microstructural constraints on
1105 the mechanisms of the transformation to reidite in naturally shocked zircon.
1106 Contributions to Mineralogy and Petrology.
1107 Erickson, T.M., Pearce, M.A., Taylor, R.J.M., Timms, N.E., Clark, C., Reddy, S.M.
1108 and Buick, I.S., 2015. Deformed monazite yields high-temperature tectonic
1109 ages. Geology, 43(5): 383-386.
1110 Erickson, T.M., Timms, N.E., Kirkland, C.L., Tohver, E., Cavosie, A.J., Pearce, M.
1111 and Reddy, S.M., in review. Shocked monazite chronometry: integrating
1112 microstructural and in situ isotopic age data for determining precise impact
1113 ages. Contributions to Mineralogy and Petrology.
1114 Farnan, I., Balan, E., Pickard, C.J. and Mauri, F., 2003. The effect of radiation
1115 damage on local structure in the crystalline fraction of $ZrSiO_4$: Investigating
1116 the 29Si NMR response to pressure in zircon and reidite. American
1117 Mineralogist, 88: 11-12.
1118 Farthing, D.J. and Pivarunas, A., 2015. GSA Abstr. with Prog., 47(7): 758.

1119 Fenner, C.N., 1913. The stability relations of the silica minerals. American Journal of
1120 Science, 214: 331-384.
1121 Flórez, M., Contreras-García, J., Recio, J.M. and Marques, M., 2009. Quantum-
1122 mechanical calculations of zircon to scheelite transition pathways in $ZrSiO_4$.
1123 Physical Review B, 79(10): 104101.
1124 Flowers, R.M., Moser, D.E. and Hart, R.J., 2003. Evolution of the Amphibolite-
1125 Granulite Facies Transition Exposed by the Vredefort Impact Structure,
1126 Kaapvaal Craton, South Africa. The Journal of geology, 111(4): 455-470.
1127 Gervasoni, F., Klemme, S., Rocha-Júnior, E.R.V. and Berndt, J., 2016. Zircon
1128 saturation in silicate melts: a new and improved model for aluminous and
1129 alkaline melts. Contributions to Mineralogy and Petrology, 171(3).
1130 Glass, B.P. and Liu, S., 2001. Discovery of high-pressure $ZrSiO_4$ polymorph in
1131 naturally occurring shock-metamorphosed zircons. Geology, 29(4): 371-373.
1132 Grange, M., Nemchin, A., Pidgeon, R., Timms, N., Muhling, J. and Kennedy, A.,
1133 2009. Thermal history recorded by the Apollo 17 impact melt breccia 73217.
1134 Geochimica Et Cosmochimica Acta, 73(10): 3093-3107.
1135 Grange, M.L., Nemchin, A.A. and Pidgeon, R.T., 2013a. The effect of 1.9 and 1.4 Ga
1136 impact events on 4.3 Ga zircon and phosphate from an Apollo 15 melt breccia.
1137 Journal of Geophysical Research: Planets, 118(10): 2180-2197.
1138 Grange, M.L., Pidgeon, R.T., Nemchin, A.A., Timms, N.E. and Meyer, C., 2013b.
1139 Interpreting U–Pb data from primary and secondary features in lunar zircon.
1140 Geochimica et Cosmochimica Acta, 101: 112-132.
1141 Grattan-Bellew, P.E., 1978. Quartz–tridymite transition under hydrothermal
1142 conditions. Explorations Mineralogiques, 11: 128-139.

1143 Grieve, R.A.F., 1975. Petrology and chemistry of the impact melt at Mistastin Lake
1144 crater, Labrador. Geological Society of America Bulletin, 86(12): 1617-1629.
1145 Gucsik, A., Koeberl, C., Brandstätter, F., Reimold, W.U. and Libowitzky, E., 2002.
1146 Cathodoluminescence, electron microscopy, and Raman spectroscopy of
1147 experimentally shock-metamorphosed zircon. Earth and Planetary Science
1148 Letters, 202(2): 495-509.
1149 Hacker, B.R., Ratschbacher, L., Webb, L., Ireland, T., Walker, D. and Shuwen, D.,
1150 1998. U/Pb zircon ages constrain the architecture of the ultrahigh-pressure
1151 Qinling–Dabie Orogen, China. Earth and Planetary Science Letters, 161(1):
1152 215-230.
1153 Haines, J., Léger, J.M. and Atouf, A., 1995. Crystal structure and equation of state of
1154 cotunnite-type zirconia. Journal of the American Ceramic Society, 78(2): 445-
1155 448.
1156 Haines, J., Léger, J.M., Hull, S., Petitet, J.P., Pereira, A.S., Perottoni, C.A. and
1157 Jornada, J.A., 1997. Characterization of the cotunnite-type phases of zirconia
1158 and hafnia by neutron diffraction and Raman spectroscopy. Journal of the
1159 American Ceramic Society, 80(7): 1910-1914.
1160 Hamann, C., Stöffler, D. and Reimold, W.U., in press. Interaction of aluminum
1161 projectiles with quartz sand in impact experiments: formation of khatyrkite
1162 ($CuAl_2$) and reduction of SiO_2 to Si. Geochimica et Cosmochimica Acta, 192:
1163 295-317.
1164 Harley, S.L., Kelly, N.M. and Möller, A., 2007. Zircon behaviour and the thermal
1165 histories of mountain chains. Elements, 3: 25-30.

1166 Hawkesworth, C.J. and Kemp, A.I.S., 2006. Using hafnium and oxygen isotopes in
1167 zircons to unravel the record of crustal evolution. Chemical Geology, 226(3-
1168 4): 144-162.
1169 Hazen, R.M. and Finger, L.W., 1979. Crystal structure and compressibility of zircon
1170 at high pressure. American Mineralogist, 64: 196-201.
1171 Heuer, A.H., Chaim, R., & Lanteri, V., 1987. The displacive cubic→ tetragonal
1172 transformation in ZrO_2 alloys. Acta Metallurgica, 35(3): 661-666.
1173 Hill, R.J. and Cranswick, L.M.D., 1994. International Union of Crystallography
1174 commission on powder difraction Rietveld refinement round robin. II.
1175 Analysis of monoclinic ZrO_2. Journal of Applied Crystallography, 27: 802-
1176 844.
1177 Holland, K.G. and Ahrens, T.J., 1997. Melting of $(Mg, Fe)_2SiO_4$ at the core-mantle
1178 boundary of the Earth. Science, 275(5306): 1623-1625.
1179 Humbert, M., Gey, N., Patapy, C., Joussein, E., Huger, M., Guinebretière, R.,
1180 Chotard, T. and Hazotte, A., 2010. Identification and orientation determination
1181 of parent cubic domains from electron backscattered diffraction maps of
1182 monoclinic pure zirconia. Scripta Materialia, 63(4): 411-414.
1183 Jackson, I., 1976. Melting of the silica isotypes SiO_2, BeF_2 and GeO_2 at elevated
1184 pressures. Physics of the Earth and Planetary Interiors, 13: 218-231.
1185 Jocelyn, J. and Pidgeon, R.T., 1974. Examples of twinning and parallel growth in
1186 zircons from some Precambrian granites and gneisses. Mineralogical
1187 Magazine, 39: 587-594.
1188 Jourdan, F., Reimold, W.U. and Deutsch, A., 2012. Dating terrestrial impact
1189 structures. Elements, 8(1): 49-53.

1190 Kaczmarek, M.A., Reddy, S.M. and Timms, N.E., 2011. Evolution of zircon
1191 deformation mechanisms in a shear zone (Lanzo massif, Western-Alps).
1192 Lithos, 127(3-4): 414-426.
1193 Kaiser, A., Lobert, M. and Telle, R., 2008. Thermal stability of zircon ($ZrSiO_4$).
1194 Journal of the European Ceramic Society, 28(11): 2199-2211.
1195 Kamo, S.L. and Krogh, T.E., 1995. Chicxulub crater source for shocked zircon
1196 crystals from the Cretaceous-Tertiary boundary layer, Saskatchewan:
1197 Evidence from new U-Pb data. Geology, 23(3): 281-284.
1198 Kamo, S.L., Reimold, W.U., Krogh, T.E. and Colliston, W.P., 1996. A 2.023 Ga age
1199 for the Vredefort impact event and a first report of shock metamorphosed
1200 zircons in pseudotachylitic breccias and granophyre. Earth and Planetary
1201 Science Letters, 144(3): 369-387.
1202 Kanzaki, M., 1990. Melting of silica up to 7 GPa. Journal of the American Ceramic
1203 Society, 73(12): 3706-3707.
1204 Kennedy, G.C., Wasserburg, G.J., Heard, H.C. and Newton, R.C., 1962. The upper
1205 three-phase region in the system SiO_2-H_2O. American Journal of Science,
1206 260(7): 501-521.
1207 Kerschhofer, L., Schärer, U. and Deutsch, A., 2000. Evidence for crystals from the
1208 lower mantle: baddeleyite megacrysts of the Mbuji Mayi kimberlite. Earth and
1209 Planetary Science Letters, 179(2): 219-225.
1210 Kieffer, S.W., Phakey, P.P. and Christie, J.M., 1976. Shock processes in porous
1211 quartzite: Transmission electron microscope observations and theory.
1212 Contributions to Mineralogy and Petrology, 59(1): 41-93.
1213 Kirfe, A., Will, G. and Arndt, J., 1979. A new phase of coesite SiO_2. Zeitschrift fur
1214 Kristallographie, 149: 315-326.

Knittle, E. and Williams, Q., 1993. High-pressure Raman spectroscopy of $ZrSiO_4$; observation of the zircon to scheelite transition at 300K. American Mineralogist, 78(3-4): 245-252.

Korhonen, F.J., Clark, C., Brown, M., Bhattacharya, S. and Taylor, R., 2013. How long-lived is ultrahigh temperature (UHT) metamorphism? Constraints from zircon and monazite geochronology in the Eastern Ghats orogenic belt, India. Precambrian Research, 234: 322-350.

Korhonen, F.J., Clark, C., Brown, M. and Taylor, R.J.M., 2014. Taking the temperature of Earth's hottest crust. Earth and Planetary Science Letters, 408: 341-354.

Kovaleva, E., Klötzli, U. and Habler, G., 2016. On the geometric relationship between deformation microstructures in zircon and the kinematic framework of the shear zone. Lithos, 262: 192-212.

Kovaleva, E., Klötzli, U., Habler, G. and Wheeler, J., 2015. Planar microstructures in zircon from paleo-seismic zones. American Mineralogist, 100(8-9): 1834-1847.

Krogh, T.E., Kamo, S.L. and Bohor, B.F., 1993a. Fingerprinting the K/T impact site and determining the time of impact by U Pb dating of single shocked zircons from distal ejecta. Earth and Planetary Science Letters, 119(3): 425-429.

Krogh, T.E., Kamo, S.L., Sharpton, V.L., Marin, L.E. and Hildebrands, A.R., 1993b. U-Pb ages of single shocked zircons linking distal K/T ejecta to the Chicxulub crater. Nature, 366: 731-734.

Kusaba, K., Takehiko Yagi, Masae Kikuchi and Syono, Y., 1986. Structural considerations on the mechanism of the shock-induced zircon-scheelite

transition in $ZrSiO_4$. Journal of Physics and Chemistry of Solids, 47(7): 675-679.

Kusaba, K., Yasuhiko Syono, M.K. and Fukuoka., K., 1985. Shock behavior of zircon: Phase transition to scheelite structure and decomposition. Earth and Planetary Science Letters, 72(4): 433-439.

Lang, M., Zhang, F., Lian, J., Trautmann, C., Neumann, R. and Ewing, R.C., 2008. Irradiation-induced stabilization of zircon ($ZrSiO_4$) at high pressure. Earth and Planetary Science Letters, 269(1-2): 291-295.

Leroux, H., Reimold, W.U., Koerberl, C., Hornemann, U. and Doukan, J.-C., 1999. Experimental shock deformation in zircon: a transmission electron microscopy study. Earth and Planetary Science Letters, 169: 291-301.

Liu, L.G., 1979. High-pressure phase transformations in baddeleyite and zircon, with geophysical implications. Earth and Planetary Science Letters, 44(3): 390-396.

Lussier, A.J., Rouvimov, S., Burns, P.C. and Simoneti, A., in press. Nuclear-blast induced nanotextures in quartz and zircon within Trinitite. American Mineralogist.

MacDonald, J.M., Wheeler, J., Harley, S.L., Mariani, E., Goodenough, K.M., Crowley, Q. and Tatham, D., 2013. Lattice distortion in a zircon population and its effects on trace element mobility and U–Th–Pb isotope systematics: examples from the Lewisian Gneiss Complex, northwest Scotland. Contributions to Mineralogy and Petrology, 166(1): 21-41.

Macris, C.A., Badro, J., Asimow, P.D., Eiler, J.M. and Stolper, E.D., 2014. Seconds after Impact: Insights from Diffusion between Lechatelierite and Host Glass in Tektites and Experiments. Meteoritics & Planetary Science, 49: A5-A454.

1263 Mao, H., Sundman, B., Wang, Z. and Saxena, S.K., 2001. Volumetric properties and
1264 phase relations of silica—thermodynamic assessment. Journal of Alloys and
1265 Compounds, 327(1): 253-262.
1266 Marion, C.L., 2009. Geology, distribution and geochemistry of impact melt at the
1267 Mistastin Lake impact crater, Labrador. Master of Science Thesis, Memorial
1268 University of Newfoundland, St John's, Newfoundland.
1269 Marion, C.L. and Sylvester, P.J., 2010. Composition and heterogeneity of anorthositic
1270 impact melt at Mistastin Lake crater, Labrador. Planetary and Space Science,
1271 58(4): 552-573.
1272 Marqués, M., Contreras-García, J., Flórez, M. and Recio, J.M., 2008. On the
1273 mechanism of the zircon-reidite pressure induced transformation. Journal of
1274 Physics and Chemistry of Solids, 69(9): 2277-2280.
1275 Marqués, M., Flórez, M., Recio, J.M., Gerward, L. and Olsen, J.S., 2006. Structure
1276 and stability of $ZrSiO_4$ under hydrostatic pressure. Physical Review B, 74(1):
1277 014104.
1278 Mashimo, T., Nagayama, K. and Sawaoka, A., 1983. Shock compression of zirconia
1279 ZrO_2 and zircon $ZrSiO_4$ in the pressure range up to 150 GPa. Physics and
1280 Chemistry of Minerals, 9(6): 237-247.
1281 McLaren, A.C., Fitz Gerald, J.D. and Williams, I.S., 1994. The microstructure of
1282 zircon and its influence on the age determination from Pb/U isotopic ratios
1283 measured by ion microprobe. Geochimica et Cosmochimica Acta, 58(2): 993-
1284 1005.
1285 Meyer, C., Jébrak, M., Stöffler, D. and Riller, U., 2011. Lateral transport of suevite
1286 inferred from 3D shape-fabric analysis: Evidence from the Ries impact crater,
1287 Germany. Geological Society of America Bulletin, 123(11-12): 2312-2319.

1288 Mirwald, P.W. and Massonne, H.J., 1980. The low-high quartz and quartz-coesite
1289 transition to 40 kbar between 600° and 1600° C and some reconnaissance data
1290 on the effect of $NaAlO_2$ component on the low quartz-coesite transition.
1291 Journal of Geophysical Research: Solid Earth, 85(B12): 6983-6990.
1292 Mittal, R., Chaplot, S.L., Choudhury, N. and Loong, C.K., 1998. Thermodynamic
1293 properties and equation of state of zircon ZrSiO4, No. ANL/IPNS/CP--92686;
1294 CONF-971158--, Argonne National Lab., IL (United States).
1295 Montalvo, S.D., Cavosie, A.J., Erickson, T.M. and Talavera, C., in press. Fluvial
1296 transport of impact evidence from cratonic interior to passive margin:
1297 Vredefort-derived shocked zircon on the Atlantic coast of South Africa.
1298 American Mineralogist, in press.
1299 Morozova, I., 2015. Strength study of zircon under high pressure. MSc thesis Thesis,
1300 The University of Western Ontario, University of Western Ontario -
1301 Electronic Thesis and Dissertation Repository, 112 pp pp.
1302 Moser, D.E., 1997. Dating the shock wave and thermal imprint of the giant Vredefort
1303 impact, South Africa. Geology, 25(1): 7-10.
1304 Moser, D.E., Cupelli, C.L., Barker, I.R., Flowers, R.M., Bowman, J.R., Wooden, J.
1305 and Hart, J.R., 2011. New zircon shock phenomena and their use for dating
1306 and reconstruction of large impact structures revealed by electron nanobeam
1307 (EBSD, CL, EDS) and isotopic U–Pb and (U–Th)/He analysis of the Vredefort
1308 dome. Canadian Journal of Earth Sciences, 48(2): 117-139.
1309 Moser, D.E., Davis, W.J., Reddy, S.M., Flemming, R.L. and Hart, R.J., 2009. Zircon
1310 U–Pb strain chronometry reveals deep impact-triggered flow. Earth and
1311 Planetary Science Letters, 277(1-2): 73-79.

Nemchin, A., Timms, N., Pidgeon, R., Geisler, T., Reddy, S. and Meyer, C., 2009. Timing of crystallization of the lunar magma ocean constrained by the oldest zircon. Nature Geoscience, 2(2): 133-136.

O'Neill, H.S.C., 2006. Free energy of formation of zircon and hafnon. American Mineralogist, 91(7): 1134-1141.

Ohtaka, O., Yamanaka, T., Kume, S., Ito, E. and Navrotsky, A., 1991. Stability of Monoclinic and Orthorhombic Zirconia: Studies by High-Pressure Phase Equilibria and Calorimetry. Journal of the American Ceramic Society, 74(3): 505-509.

Ohtaka, O., Yamanaka, T. and Yagi, T., 1994. New high-pressure and-temperature phase of ZrO_2 above 1000 °C at 20 GPa. Physical Review B, 49(14): 9295-9298.

Ono, S., Funakoshi, K., Nakajima, Y., Tange, Y. and Katsura, T., 2004a. Phase transition of zircon at high P-T conditions. Contributions to Mineralogy and Petrology, 147(4): 505-509.

Ono, S., Tange, Y., Katayama, I. and Kikegawa, T., 2004b. Equations of state of $ZrSiO_4$ phases in the upper mantle. American Mineralogist, 89(1): 185-188.

Onorato, P.I.K., Uhlmann, D.R. and Simonds, C.H., 1978. The thermal history of the Manicouagan impact melt sheet, Quebec. Journal of Geophysical Research: Solid Earth, 83(B6): 2789-2798.

Ortiz, A.L., Sánchez-González, J., González-Méndez, L.M. and Cumbrera, F.L., 2007. Determination of the thermal stability and isothermal bulk modulus of the ZrO_2 polymorphs at room temperature by molecular dynamics with a semi-empirical quantum-chemical model. Ceramics International, 33(5): 705-709.

Ostrovsky, I.A., 1966. PT-diagram of the system SiO_2-H_2O. Geological Journal, 5: 127-134.

Pacalo, R.E.G. and Gasparik, T., 1990. Reversals of the orthoenstatite-clinoenstatite transition at high pressures and high temperatures. Journal of Geophysical Research: Solid Earth, 95(B10): 15853-15858.

Peterman, E.M., Reddy, S.M., Saxey, D.W., Snoeyenbos, D.R., Rickard, W.D., Fougerouse, D. and Kylander-Clark, A.R., 2016. Nanogeochronology of discordant zircon measured by atom probe microscopy of Pb-enriched dislocation loops. Science Advances, 2(9): e1601318.

Piazolo, S., Austrheim, H. and Whitehouse, M., 2012. Brittle-ductile microfabrics in naturally deformed zircon: Deformation mechanisms and consequences for U-Pb dating. American Mineralogist, 97(10): 1544-1563.

Piazolo, S., La Fontaine, A., Trimby, P., Harley, S., Yang, L., Armstrong, R. and Cairney, J.M., 2016. Deformation-induced trace element redistribution in zircon revealed using atom probe tomography. Nature Communications, 7: 10490.

Prior, D.J., Boyle, A.P., Brenker, F., Cheadle, M.C., Day, A., Lopez, G., Peruzzo, L., Potts, G.J., Reddy, S., Spiess, R., Timms, N.E., Trimby, P., Wheeler, J. and Zetterström, L., 1999. The application of electron backscatter diffraction and orientation contrast imaging in the SEM to textural problems in rocks. American Mineralogist, 84: 1741-1759.

Reddy, S.M., Johnson, T.E., Fischer, S., Rickard, W.D.A. and Taylor, R.J.M., 2015. Precambrian reidite discovered in shocked zircon from the Stac Fada impactite, Scotland. Geology, 43(10): 899-902.

1361 Reddy, S.M., Timms, N.E. and Eglington, B.M., 2008. Electron backscatter
1362 diffraction analysis of zircon: A systematic assessment of match unit
1363 characteristics and pattern indexing optimization. American Mineralogist,
1364 93(1): 187-197.
1365 Reddy, S.M., Timms, N.E., Hamilton, P.J. and Smyth, H.R., 2009. Deformation-
1366 related microstructures in magmatic zircon and implications for diffusion.
1367 Contributions to Mineralogy and Petrology, 157(2): 231-244.
1368 Reddy, S.M., Timms, N.E., Pantleon, W. and Trimby, P., 2007. Quantitative
1369 characterization of plastic deformation of zircon and geological implications.
1370 Contributions to Mineralogy and Petrology, 153(6): 625-645.
1371 Reddy, S.M., Timms, N.E., Trimby, P., Kinny, P.D., Buchan, C. and Blake, K., 2006.
1372 Crystal-plastic deformation of zircon: A defect in the assumption of chemical
1373 robustness. Geology, 34(4): 257-260.
1374 Reddy, S.M., van Riessen, A., Saxey, D.W., Johnson, T.E., Rickard, W.D.,
1375 Fougerouse, D., Fischer, S., Prosa, T.J., Rice, K.P., Reinhard, D.A. and Chen,
1376 Y., 2016. Mechanisms of deformation-induced trace element migration in
1377 zircon resolved by atom probe and correlative microscopy. Geochimica et
1378 Cosmochimica Acta, 195: 158-170.
1379 Reid, A.F. and Ringwood, A.E., 1969. Newly observed high pressure transformations
1380 in Mn_3O_4, $CaAl_2O_4$, and $ZrSiO_4$. Earth and Planetary Science Letters, 6: 205-
1381 208.
1382 Reimold, W.U., Hansen, B.K., Jacob, J., Artemieva, N.A., Wunnemann, K. and
1383 Meyer, C., 2011. Petrography of the impact breccias of the Enkingen (SUBO
1384 18) drill core, southern Ries crater, Germany: New estimate of impact melt
1385 volume. Geological Society of America Bulletin, 124(1-2): 104-132.

1386 Reimold, W.U., Leroux, H. and Gibson, R.L., 2002. Shocked and thermally
1387 metamorphosed zircon from the Vredefort impact structure, South Africa: a
1388 transmission electron microscopic study. European Journal of Mineralogy,
1389 14(5): 859-868.
1390 Rimša, A., Whitehouse, M.J., Johansson, L. and Piazolo, S., 2007. Brittle fracturing
1391 and fracture healing of zircon: An integrated cathodoluminescence, EBSD, U-
1392 Th-Pb, and REE study. American Mineralogist, 92(7): 1213-1224.
1393 Robie, R.A. and Hemingway, B.S., 1995. Thermodynamic properties of minerals and
1394 related substances at 298.15 K and 1 bar (10^5 Pascals) pressure and at higher
1395 temperatures. U.S. Geological Survey Bulletin, No. 2131. United States
1396 Government Printing Office, Washington, 461 pp.
1397 Sands, D.E., 1969. Introduction to crystallography. WA Benjamin, New York, 165 pp
1398 pp.
1399 Schmieder, M., Tohver, E., Jourdan, F., Denyszyn, S.W. and Haines, P.W., 2015.
1400 Zircons from the Acraman impact melt rock (South Australia): Shock
1401 metamorphism, U–Pb and $^{40}Ar/^{39}Ar$ systematics, and implications for the
1402 isotopic dating of impact events. Geochimica et Cosmochimica Acta, 161: 71-
1403 100.
1404 Schmitt, D.R. and Ahrens, T.J., 1989. Shock temperatures in silica glass: Implications
1405 for modes of shock-induced deformation, phase transformation, and melting
1406 with pressure. Journal of Geophysical Research, 94(B5): 5851.
1407 Shoemaker, E.M. and Chao, E.C., 1961. New evidence for the impact origin of the
1408 Ries Basin, Bavaria, Germany. Journal of Geophysical Research, 66(10):
1409 3371-3378.

Singleton, A.C., Osinski, G.R. and Shieh, S.R., 2015. Microscopic effects of shock metamorphism in zircons from the Haughton impact structure, Canada. Geological Society of America Special Papers, 518: 135-148.

Smirnov, M.B., Mirgorodsky, A.P., Kazimirov, V.Y. and Guinebretière, R., 2008. Bond-switching mechanism for the zircon-scheelite phase transition. Physical Review B, 78(9): 094109.

Smith, D.K. and Newkirk, H.W., 1965. The crystal structure of baddeleyite (monoclinic ZrO_2) and its relation to the polymorphism of ZrO_2. Acta Crystallographica, 18(6): 983-991.

Stöffler, D., 1971. Progressive metamorphism and classification of shocked and brecciated crystalline rocks at impact craters. Journal of Geophysical Research, 76(23): 5541-5551.

Stöffler, D., 1977. Research drilling Nördlingen 1973: Polymict breccias, crater basement, and cratering model of the Ries impact structure. Geologica Bavarica, 75: 443-458.

Stöffler, D., Artemieva, N.A., Wünnemann, K., Reimold, W.U., Jacob, J., Hansen, B.K. and Summerson, I.A.T., 2013. Ries crater and suevite revisited-Observations and modeling Part I: Observations. Meteoritics & Planetary Science, 48(4): 515-589.

Subbarao, E.C., Agrawal, D.K., McKinstry, H.A., Sallese, C.W. and Roy, R., 1990. Thermal expansion of compounds of zircon structure. Journal of the American Ceramic Society, 73(5): 1246-1252.

Subbarao, E.C., Maiti, H.S. and Srivastava, K.K., 1974. Martensitic transformation in zirconia. Physica status solidi (a), 21(1): 9-40.

1434 Suito, K., 1977. Phase relations of pure Mg_2SiO_4 up to 200 kilobars. In: M.H.
1435 Manghnani and S. Akimoto (Editors), High-Pressure Research: Applications
1436 in Geophysics. Academic, San Diego, California, pp. 255-266.
1437 Swamy, V., Saxena, S.K., Sundman, B. and Zhang, J., 1994. A thermodynamic
1438 assessment of silica phase diagram. Journal of Geophysical Research: Solid
1439 Earth, 99(B6): 11787-11794.
1440 Sylvester, P., Crowley, J. and Schmitz, M., 2013. U–Pb zircon age of Mistastin Lake
1441 crater, Labrador, Canada–implications for high-precision dating of small
1442 impact melt sheets and the end Eocene extinction, Goldschmidt. Mineralogical
1443 Magazine, Florence, Italy, pp. 2295.
1444 Tange, Y. and Takahashi, E., 2004. Stability of the high-pressure polymorph of zircon
1445 ($ZrSiO_4$) in the deep mantle. Physics of the Earth and Planetary Interiors, 143-
1446 144: 223-229.
1447 Telle, R., Greffrath, F. and Prieler, R., 2015. Direct observation of the liquid
1448 miscibility gap in the zirconia–silica system. Journal of the European Ceramic
1449 Society, 35(14): 3995-4004.
1450 Teufer, G., 1962. The crystal structure of tetragonal ZrO_2. Acta Crystallographica,
1451 15(11): 1187.
1452 Thomson, O.A., Cavosie, A.J., Moser, D.E., Barker, I., Radovan, H.A. and French,
1453 B.M., 2014. Preservation of detrital shocked minerals derived from the 1.85
1454 Ga Sudbury impact structure in modern alluvium and Holocene glacial
1455 deposits. Geological Society of America Bulletin, 126(5-6): 720-737.
1456 Timms, N.E., Healy, D., Erickson, T.M., Nemchin, A.A. and Pearce, M.A., in review.
1457 Role of elastic anisotropy in the development of deformation microstructures
1458 in zircon. In: D. Moser, F. Corfu, S. Reddy, J. Darling and K. Tait (Editors),

AGU Monograph: Microstructural Geochronology; Lattice to Atom-scale Records of Planetary Evolution. AGU-Wiley.

Timms, N.E., Kinny, P.D. and Reddy, S.M., 2006. Enhanced diffusion of uranium and thorium linked to crystal plasticity in zircon. Geochemical Transactions, 7: 10.

Timms, N.E., Kinny, P.D., Reddy, S.M., Evans, K., Clark, C. and Healy, D., 2011. Relationship among titanium, rare earth elements, U–Pb ages and deformation microstructures in zircon: Implications for Ti-in-zircon thermometry. Chemical Geology, 280(1-2): 33-46.

Timms, N.E. and Reddy, S.M., 2009. Response of cathodoluminescence to crystal-plastic deformation in zircon. Chemical Geology, 261(1-2): 12-24.

Timms, N.E., Reddy, S.M., Gerald, J.D.F., Green, L. and Muhling, J.R., 2012a. Inclusion-localised crystal-plasticity, dynamic porosity, and fast-diffusion pathway generation in zircon. Journal of Structural Geology, 35(78-89).

Timms, N.E., Reddy, S.M., Healy, D., Nemchin, A.A., Grange, M.L., Pidgeon, R.T. and Hart, R., 2012b. Resolution of impact-related microstructures in lunar zircon: A shock-deformation mechanism map. Meteoritics & Planetary Science, 47(1): 120-141.

Tohver, E., Lana, C., Cawood, P.A., Fletcher, I.R., Jourdan, F., Sherlock, S., Rasmussen, B., Trindade, R.I.F., Yokoyama, E., Souza Filho, C.R. and Marangoni, Y., 2012. Geochronological constraints on the age of a Permo–Triassic impact event: U–Pb and $^{40}Ar/^{39}Ar$ results for the 40 km Araguainha structure of central Brazil. Geochimica et Cosmochimica Acta, 86: 214-227.

Tretiakova, I.G., Belousova, E.A., Malkovets, V.G., Griffin, W.L., Piazolo, S., Pearson, N.J., O'Reilly, S. and Nishido, H., 2016. Recurrent magmatic activity

on a lithosphere-scale structure: Crystallization and deformation in kimberlitic zircons. Gondwana Research.

Turner, D., Langenhorst, F. and Pollok, K., 2014. Martensitic Mechanism of the Zircon-to-Reidite Transformation. LPI Contributions, 1800: 5411.

Valley, J.W., Cavosie, A.J., Ushikubo, T., Reinhard, D.A., Lawrence, D.F., Larson, D.J., Clifton, P.H., Kelly, T.F., Wilde, S.A., Moser, D.E. and Spicuzza, M.J., 2014. Hadean age for a post-magma-ocean zircon confirmed by atom-probe tomography. Nature Geoscience, 7(3): 219-223.

Valley, J.W., Lackey, J.S., Cavosie, A.J., Clechenko, C.C., Spicuzza, M.J., Basei, M.A.S., Bindeman, I.N., Ferreira, V.P., Sial, A.N., King, E.M. and Peck, W.H., 2005. 4.4 billion years of crustal maturation: oxygen isotope ratios of magmatic zircon. Contributions to Mineralogy and Petrology, 150(6): 561-580.

van Westrenen, W., Frank, M.R., Hanchar, J.M., Fei, Y., Finch, R.J. and Zha, C.S., 2004. In situ determination of the compressibility of synthetic pure zircon ($ZrSiO_4$) and the onset of the zircon-reidite phase transition. American Mineralogist, 89(1): 197-203.

Wackerle, J., 1962. Shock‐wave compression of quartz. Journal of Applied Physics, 33(3): 922-937.

Watson, E.B. and Harrison, T.M., 1983. Zircon saturation revisited: temperature and composition effects in a variety of crustal magma types. Earth and Planetary Science Letters, 64(2): 295-304.

Wenk, H.R. and Weiss, L.E., 1982. Al-rich calcic pyroxene in pseudotachylite: an indicator of high pressure and high temperature? Tectonophysics, 84(2): 329-341.

1509 Wheeler, J., Prior, D., Jiang, Z., Spiess, R. and Trimby, P., 2001. The petrological
1510 significance of misorientations between grains. Contributions to Mineralogy
1511 and Petrology, 141(1): 109-124.
1512 Whitney, E.D., 1965. Electrical resistivity and diffusionless phase transformations of
1513 zirconia at high temperatures and ultrahigh pressures. Journal of the
1514 Electrochemical Society, 112(1): 91-94.
1515 Wilde, S.A., Valley, J.W., Peck, W.H. and Graham, C.M., 2001. Evidence from
1516 detrital zircons for the existence of continental crust and oceans on the Earth
1517 4.4 Gyr ago. Nature, 4009(6817): 175-178.
1518 Wilke, M., Schmidt, C., Dubrail, J., Appel, K., Borchert, M., Kvashnina, K. and
1519 Manning, C.E., 2012. Zircon solubility and zirconium complexation in
1520 $H_2O+Na_2O+SiO_2\pm Al_2O_3$ fluids at high pressure and temperature. Earth and
1521 Planetary Science Letters, 349-350: 15-25.
1522 Williams, G.E., 1986. The Acraman impact structure: Source of ejecta in late
1523 Precambrian shales, South Australia. Science, 233: 200-203.
1524 Williams, G.E., 1994. Acraman, South Australia: Australia's largest meteorite impact
1525 structure, Proceedings of the Royal Society of Victoria, pp. 105-127.
1526 Wittmann, A., Kenkmann, T., Schmitt, R.T. and Stöffler, D., 2006. Shock-
1527 metamorphosed zircon in terrestrial impact craters. Meteoritics & Planetary
1528 Science, 41(3): 433-454.
1529 Wittmann, A., Schmitt, R.T., Hecht, L., Kring, D.A., Reimold, W.U. and Povenmire,
1530 H., 2009. Petrology of impact melt rocks from the Chesapeake Bay crater,
1531 USA. Geological Society of America Special Papers, 458: 377-396.
1532 Yagi, T. and Akimoto, S.I., 1976. Direct determination of coesite-stishovite transition
1533 by in-situ X-ray measurements. Tectonophysics, 35(1): 259-270.

Yue, B., Hong, F., Merkel, S., Tan, D., Yan, J., Chen, B. and Mao, H.K., 2016. Deformation Behavior across the Zircon-Scheelite Phase Transition. Phys Rev Lett, 117(13): 135701.

Zanetti, M.R., 2015. Investigating the Complexity of Impact Crater Ejecta.

Zhang, J., 1992. Melting of mantle minerals at high pressures: Experimental study and thermodynamic evaluation, City University of New York, New York, 114 pp pp.

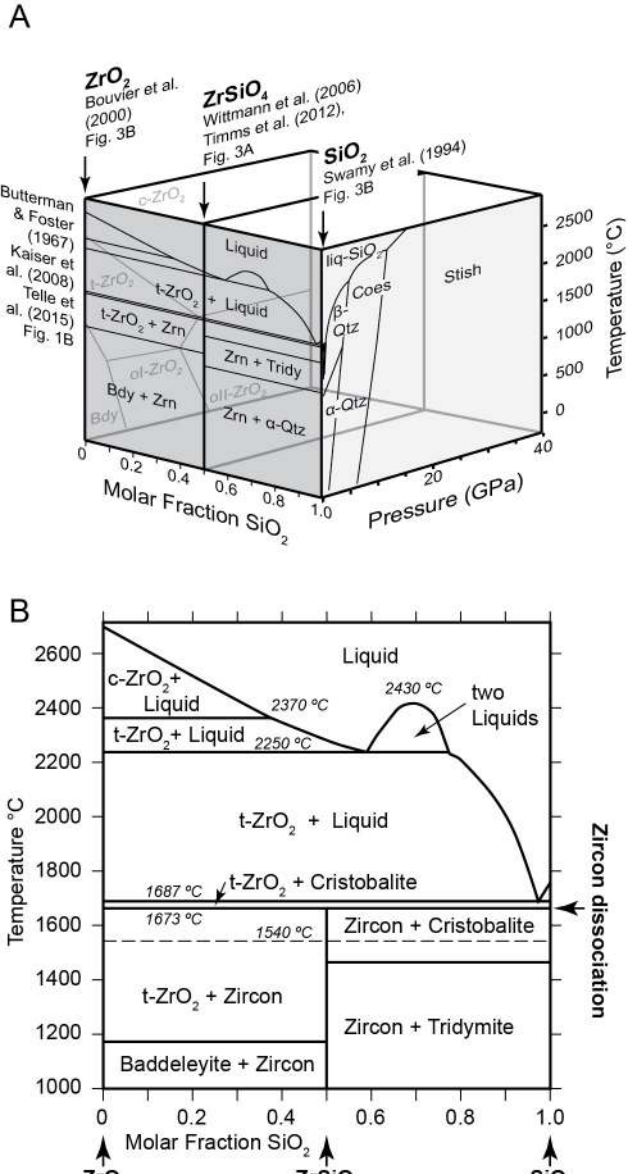

Timms et al. Figure 1

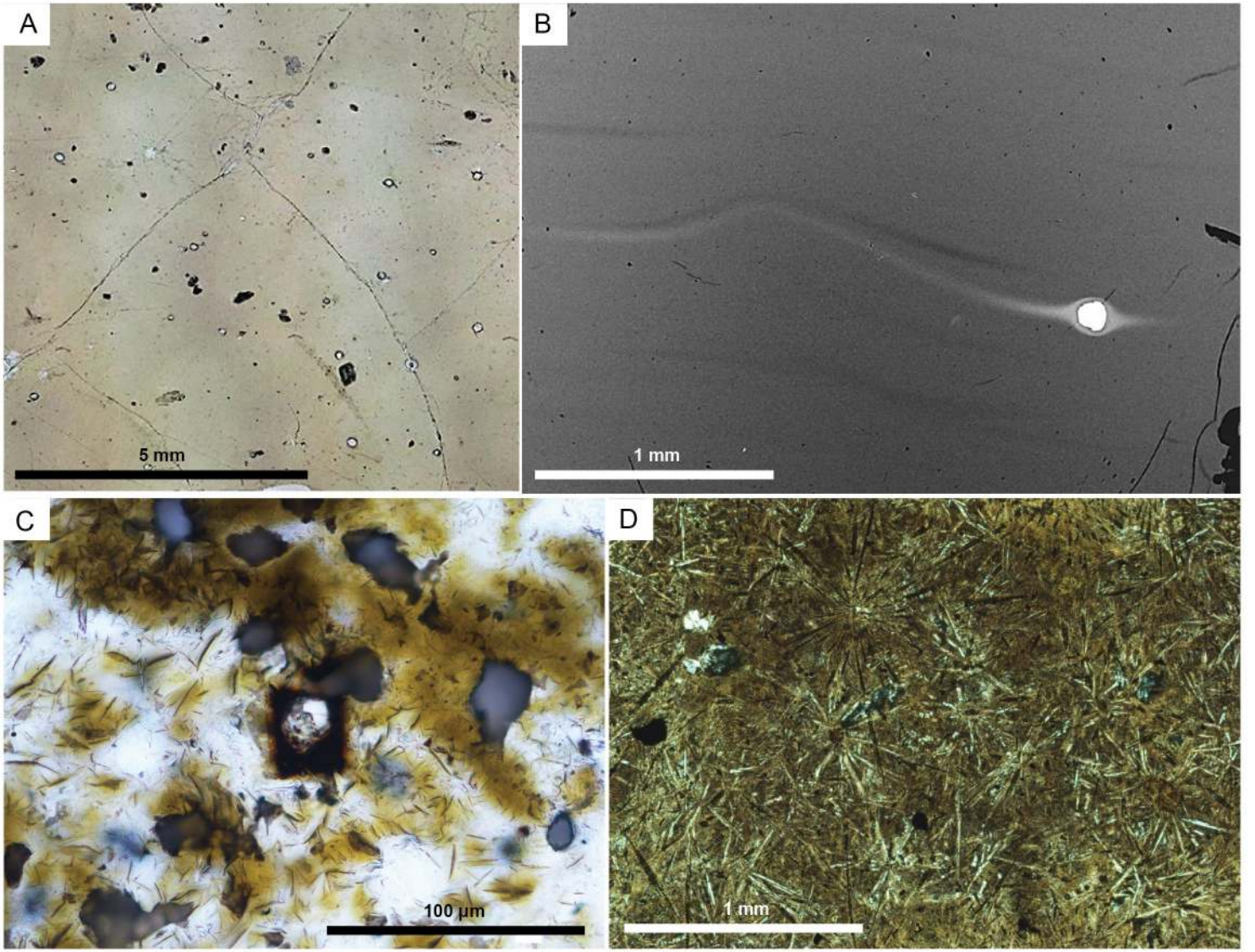

Timms et al. Figure 2

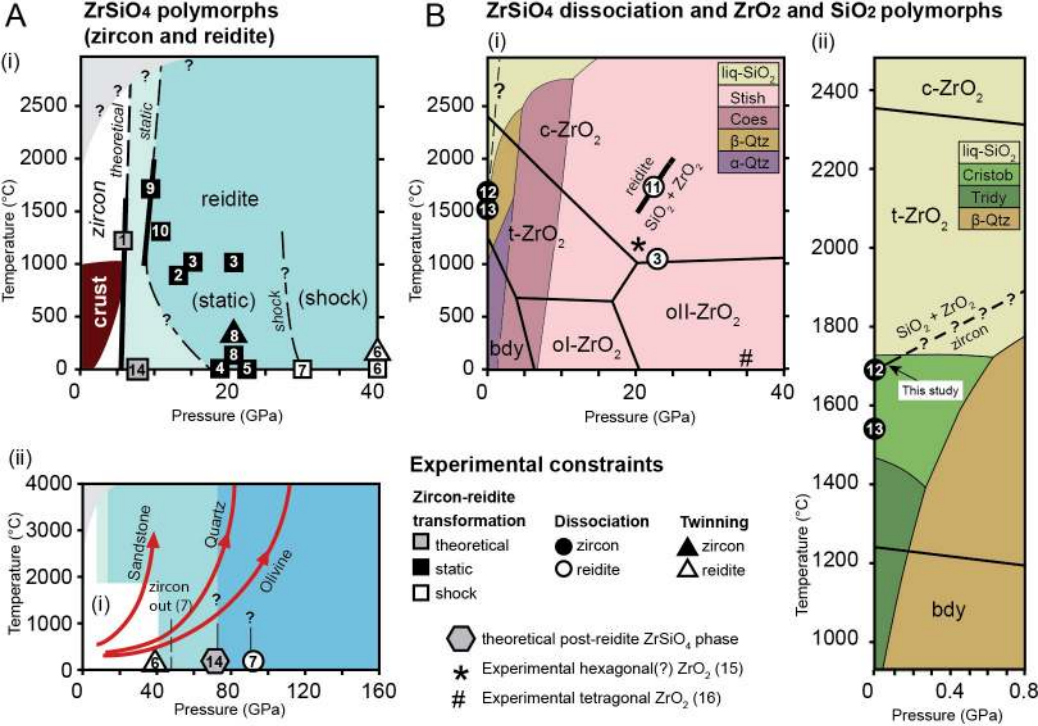

Timms et al. Figure 3

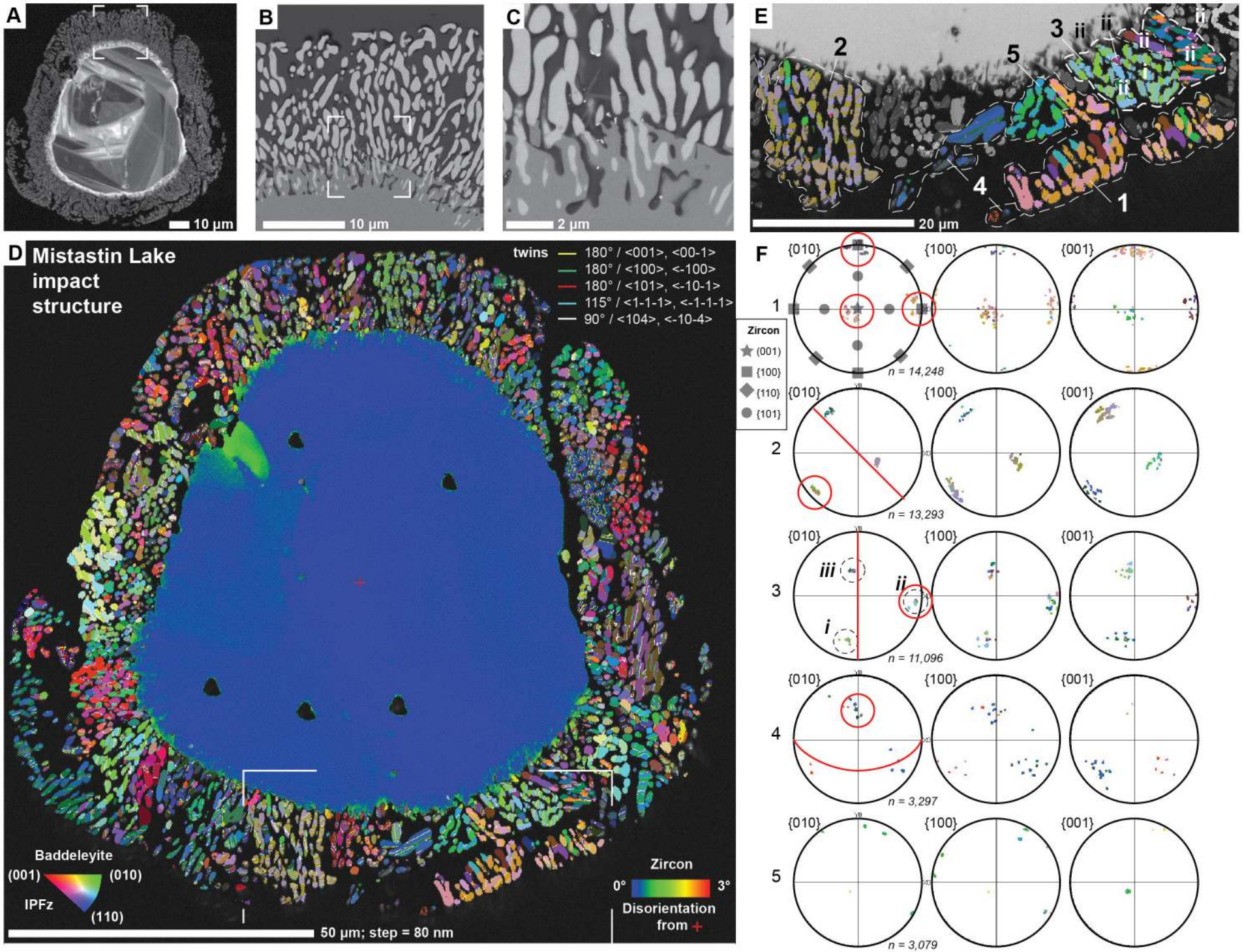

Timms et al. Figure 4

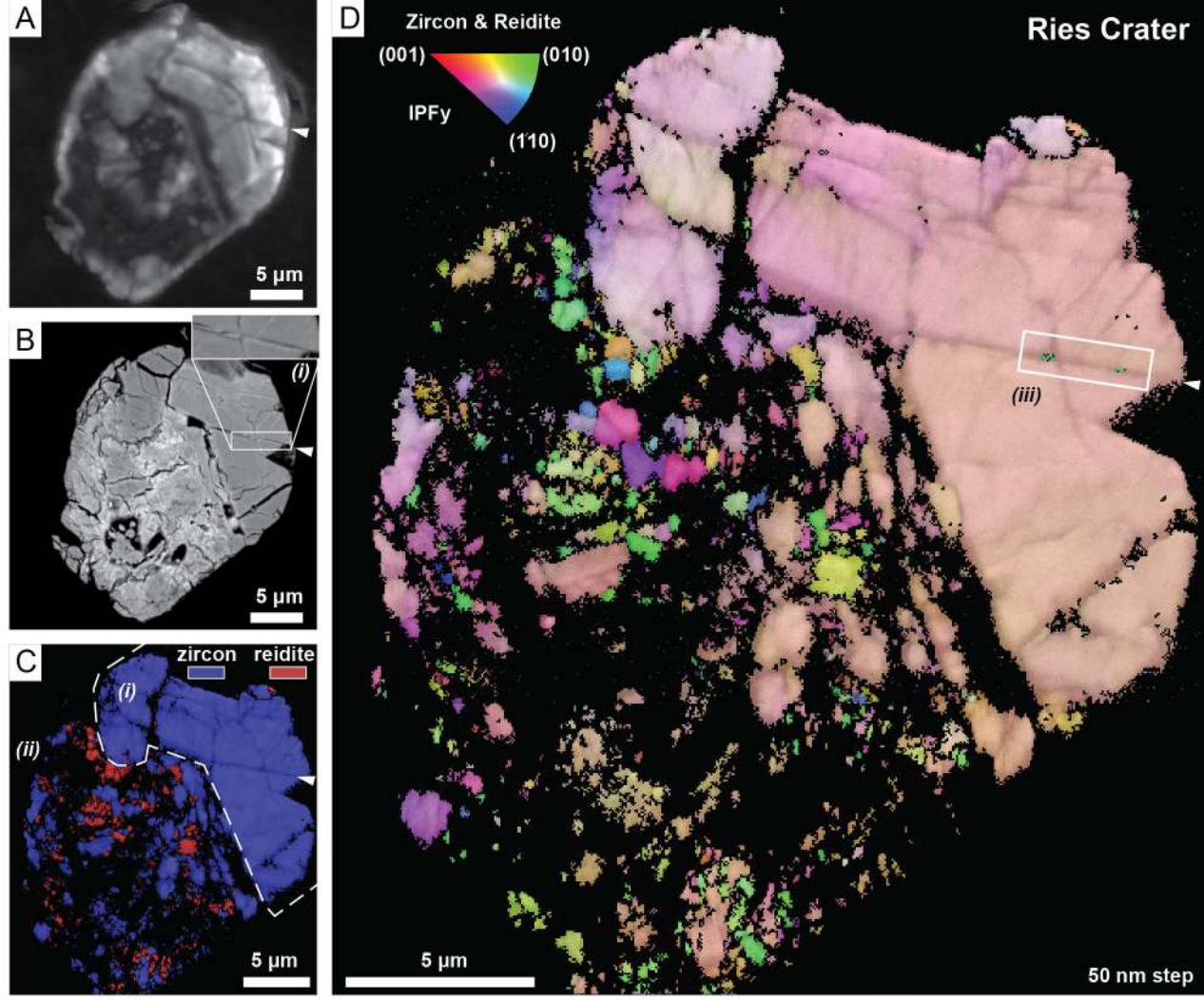

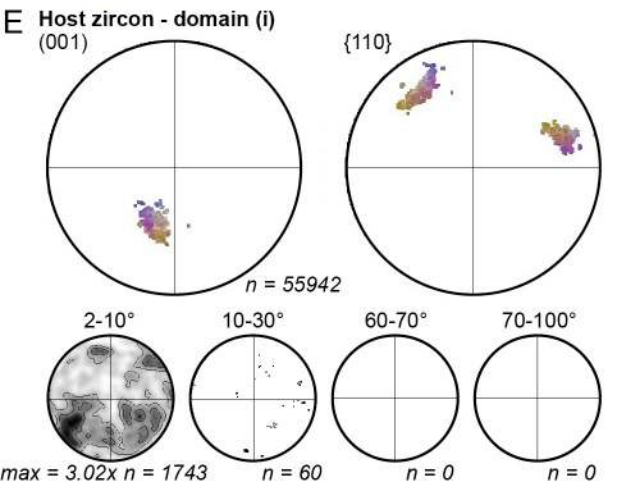

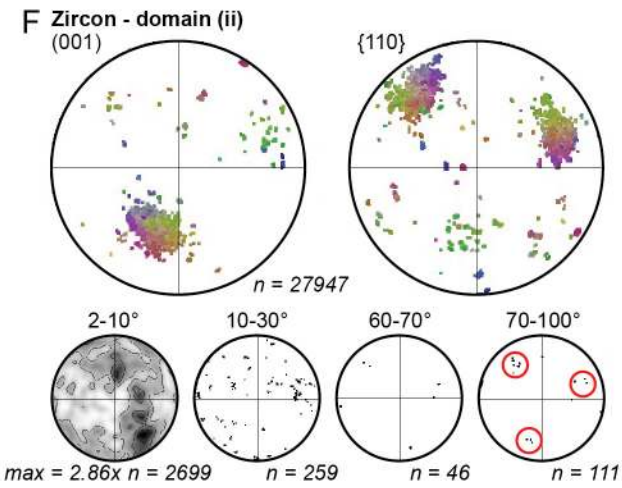

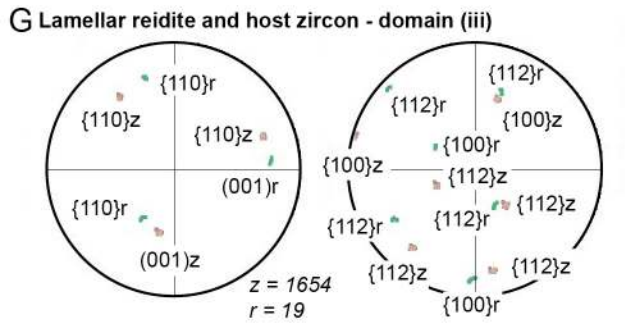

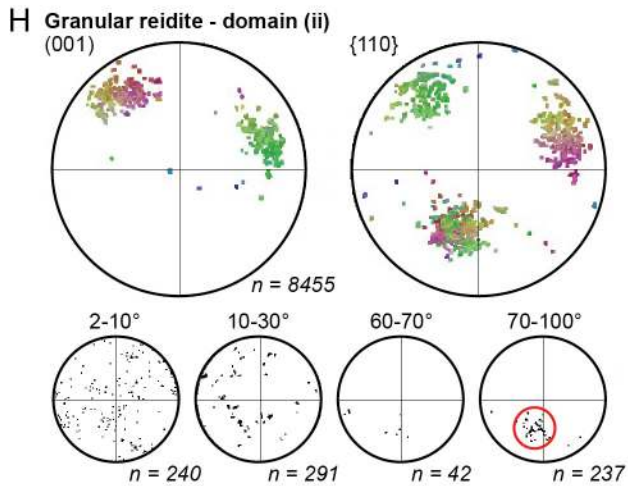

Timms et al. Figure 5

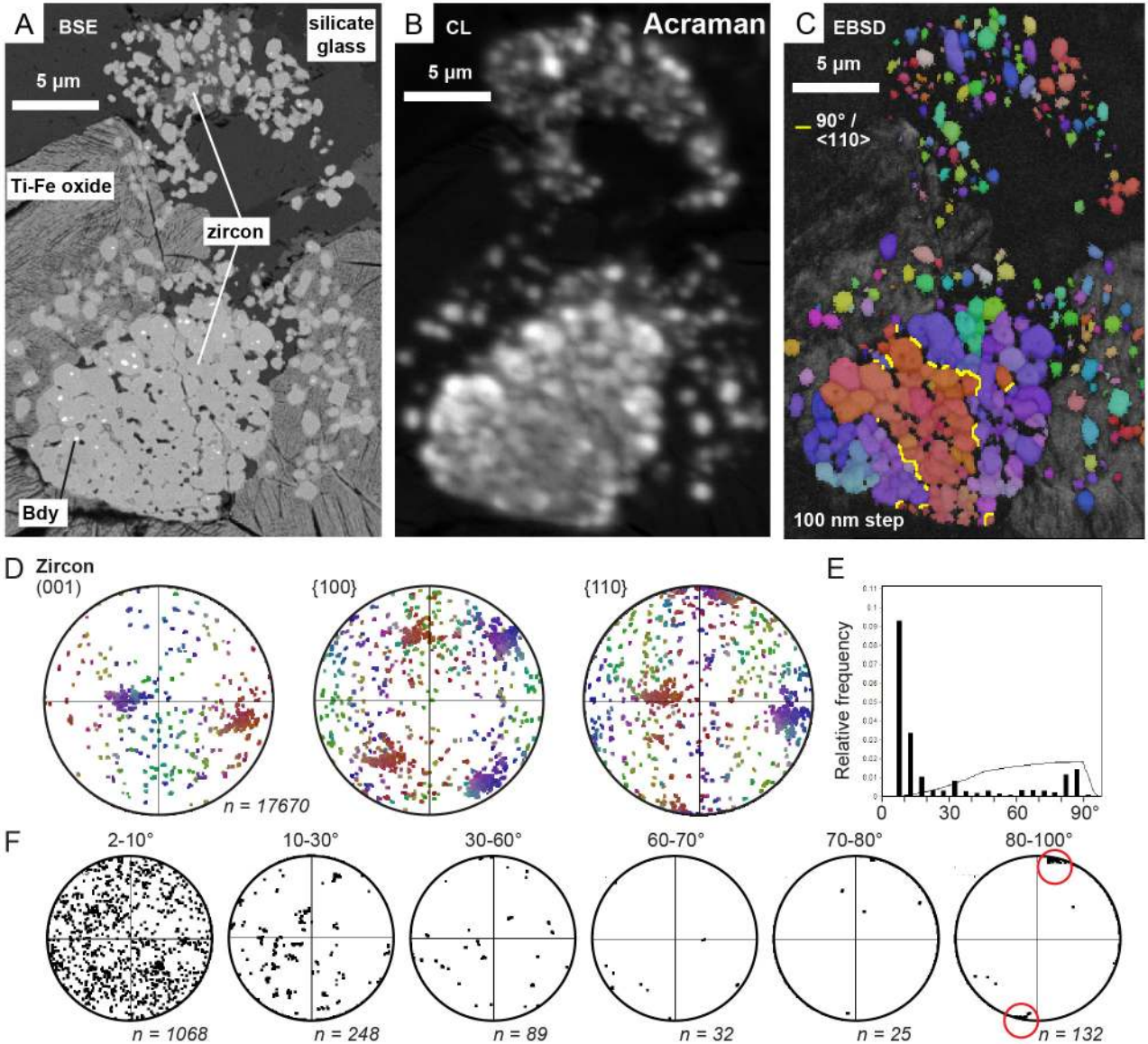

Timms et al. Figure 6

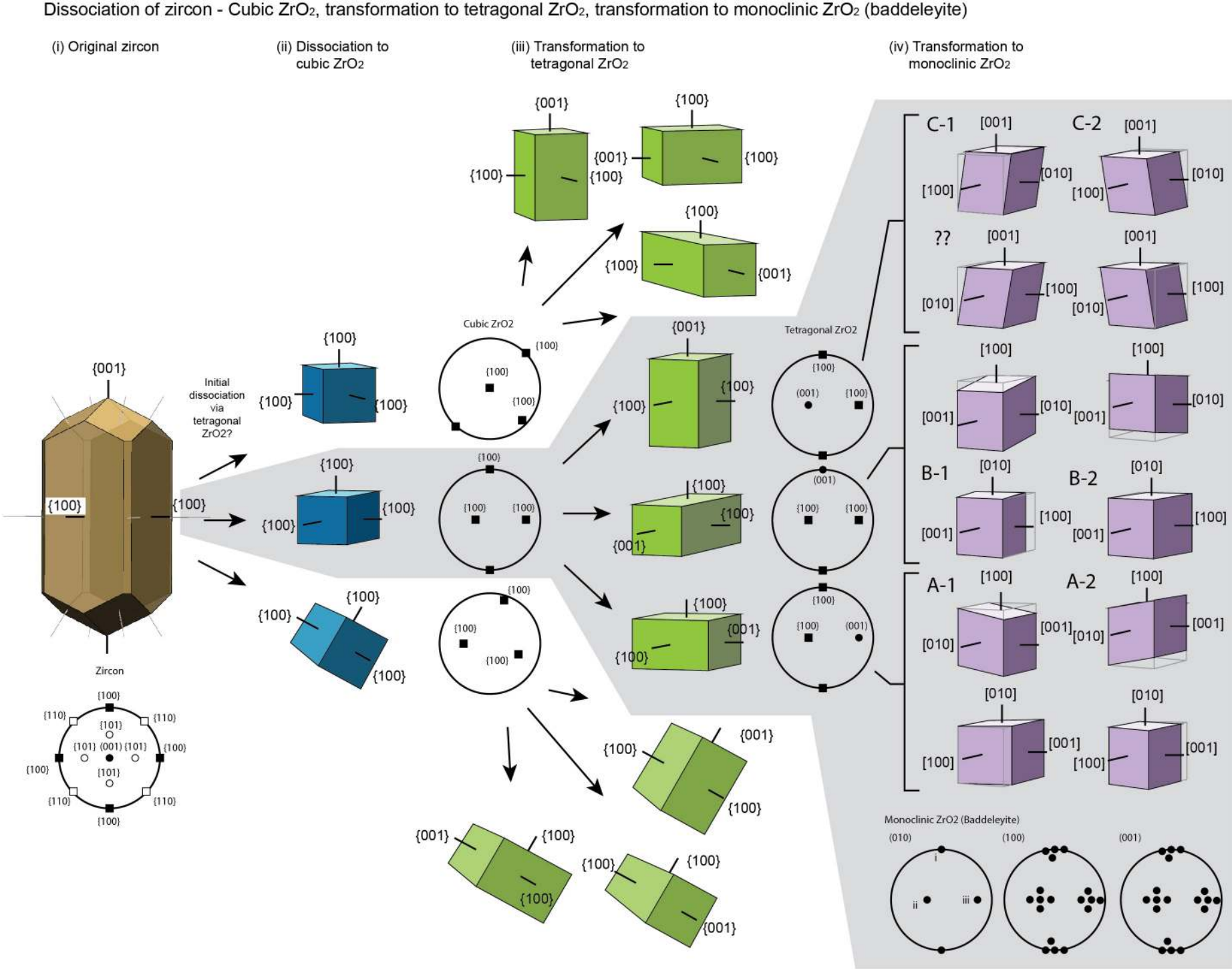

Timms et al. Figure 7

Transformation to reidite, reversion to zircon

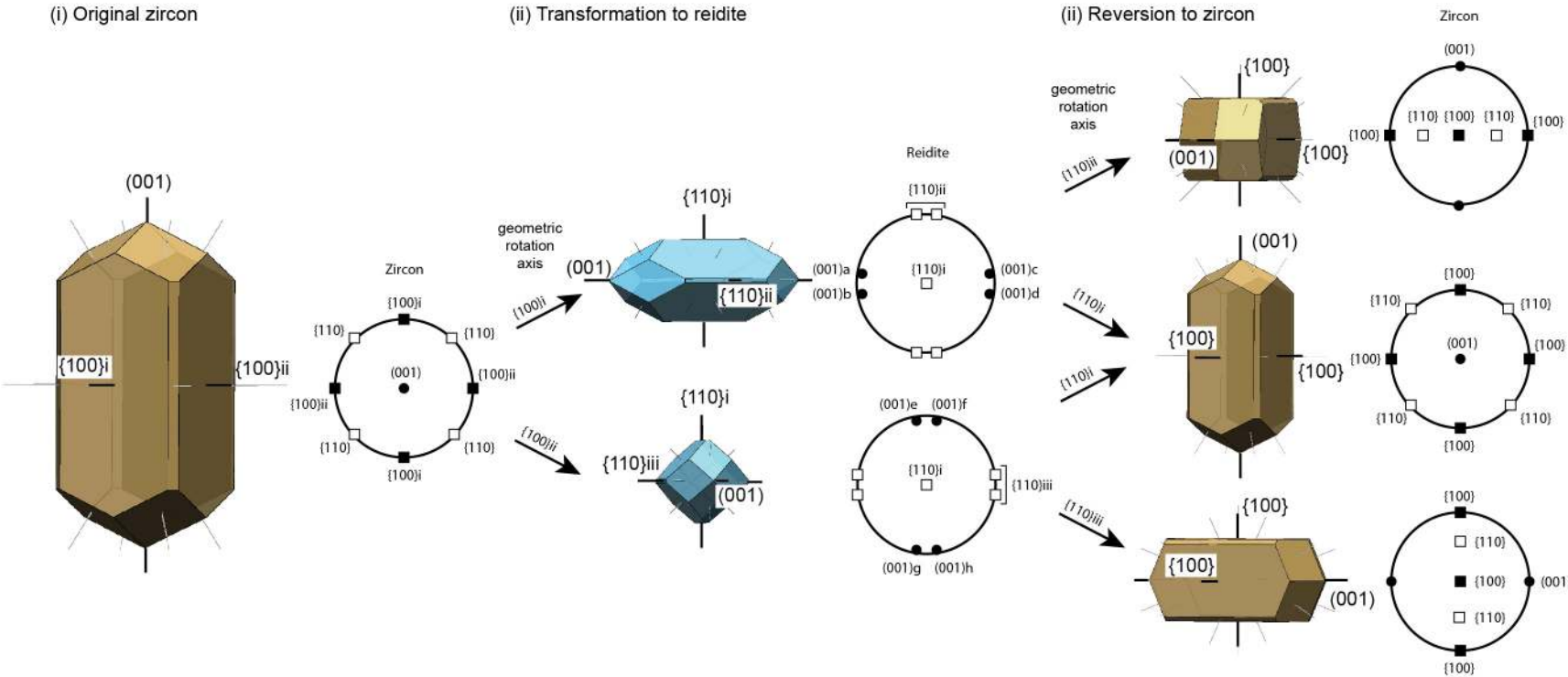

Timms et al. Figure 8

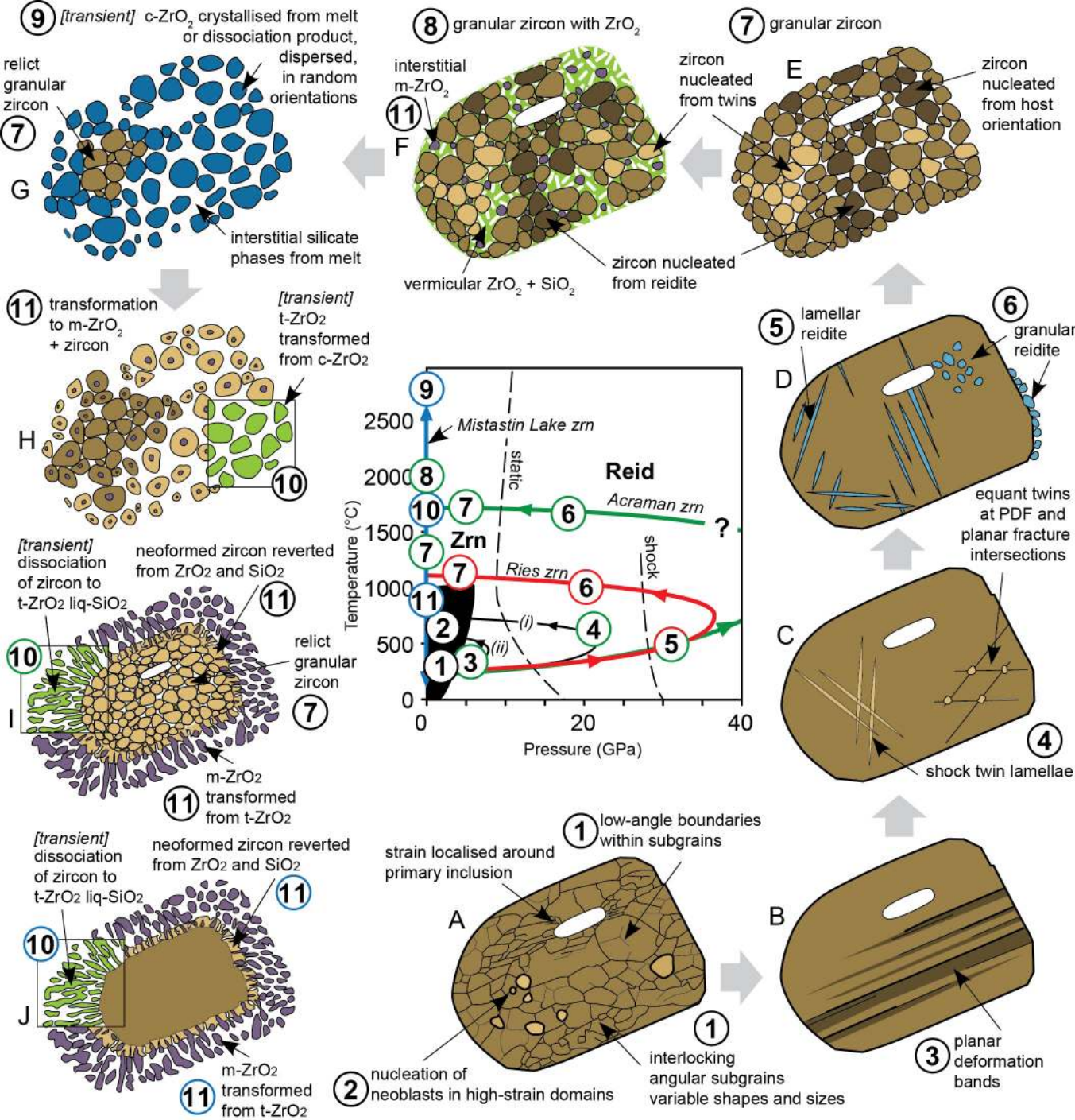

Timms et al., Figure 9

Table 1. Thermodynamic parameters used to calculate zircon dissociation reaction line. Temperature in °K. Data source references indicated by superscript letters: a = O'Neill, 2006; b = Bouvier et al., 2002; c = Robie & Hemmingway, 1995; d = Ortiz et al., 2007; e = Mao et al., 2001; f = Adams et al., 1985; g = Mittal et al. 1998; h = Subbarao et al., 1990.

Phase	δHf (1,Tref)	S(1,Tref)	Tref	A	b	c	d	V0(1,Tref)	a0	b0	Kp'
Zircon	-2034.2[a]	-384.0[a]	298.15	2.32E+02[a]	-1.44E-02[a]		-2.24E+03[a]	39.81[c]	5.00E-06[h]	4.44E-07[g]	6.5[g]
Mon-ZrO_2	-1100.6[a]	167.1[a]	298.15	1.03E+02[a]	-4.55E-03[a]	-4.16E+05[a]	-7.14E+02[a]	21.15[c]	8.12E-06[f]	5.21E-07[d]	5[d]
Tet-ZrO_2	-1009.7[a]	165.8[a]	1430	7.86E+01[a]				20[b]	9.93E-06[f]	4.83E-07[d]	4.4[d]
Cristobalite	-896.0[a]	69.7[a]	523	6.69E+01[a]	4.85E-03[a]	2.54E+06[a]		27.426[c]	1.05E-06[e]	7.47E-11[e]	6[e]

Table 2. Scanning electron microscopy settings and electron backscatter diffraction analysis acquisition and processing parameters.

SEM			
Make/model	Tescan Mira3 FEG-SEM		
EBSD acquisition system	Oxford Instruments Aztec / Nordlys EBSD Detector		
EBSD Processing software	Oxford Instruments Channel 5.10		
Acceleration Voltage (kV)	20		
Working Distance (mm)	~20.5		
Tilt	70°		
EBSD match units			
Zircon	Zircon5260, 1 atm (Hazen and Finger, 1979)		
Reidite	Reidite632, 0.69 GPa (Farnan et al., 2003)		
Baddeleyite (monoclinic ZrO_2)	(Bondars et al., 1995), (Hill and Cranswick, 1994)		
Tetragonal ZrO_2	(Teufer, 1962)		
Cubic ZrO_2	ICSD card 53998 (Böhm, 1925)		
Orthorhombic ZrO_2	ICSD card 77716		
Quartz	'Quartznew', HKL database (Sands, 1969)		
Cristobalite	(Downs and Palmer, 1994)		
Coesite	(Kirfe et al., 1979)		
EBSP Acquisition, Indexing and Processing			
Sample Location	**Mistastin Lake**	**Ries**	**Acraman**
Grain ID	Zrn 2	Zrn 21	Zrn 19
Figure	4	5	6
EBSP Acquisition Speed (Hz)	40	40	40
EBSP Background (frames)	64	64	64
EBSP Binning	4 x 4	4 x 4	4 x 4
EBSP Gain	High	High	High
Hough resolution	60	60	60
Band detection (min / max)	6 / 8	6 / 8	6 / 8
Mean angular deviation (zircon)	<1°	<1°	<1°
Mean angular deviation (reidite)	n/a	<1°	n/a
Mean angular deviation (baddeleyite)	<1°	n/a	n/a
Map step size (nm)	80	200	100
Map size (X steps / Y steps)	1495 / 1435	417 / 442	205 / 314
EBSD noise reduction routine			
Wildspike correction	Yes	Yes	Yes
Nearest neighbour zero solution extrapolation	6	7	6

References

Böhm, J., 1925. Über das Verglimmen einiger Metalloxyde. Z. Anorg. Allg. Chem., 149: 217-222.

Bondars, B., Heidemane, G., Grabis, J., Laschke, K., Boysen, H., Schneider, J. and Frey, F., 1995. Powder diffraction investigations of plasma sprayed zirconia. Journal of Materials Science, 30(6): 1621-1625.

Downs, R.T. and Palmer, D.C., 1994. The pressure behavior of c~-cristobalite. American Mineralogist, 79: 9-14.

Farnan, I., Balan, E., Pickard, C.J. and Mauri, F., 2003. The effect of radiation damage on local structure in the crystalline fraction of $ZrSiO_4$: Investigating the 29Si NMR response to pressure in zircon and reidite. American Mineralogist, 88: 11-12.

Hazen, R.M. and Finger, L.W., 1979. Crystal structure and compressibility of zircon at high pressure. American Mineralogist, 64: 196-201.

Hill, R.J. and Cranswick, L.M.D., 1994. International Union of Crystallography commission on powder difraction Rietveld refinement round robin. II. Analysis of monoclinic ZrO_2. Journal of Applied Crystallography, 27: 802-844.

Kirfe, A., Will, G. and Arndt, J., 1979. A new phase of coesite SiO_2. Zeitschrift fur Kristallographie, 149: 315-326.

Sands, D.E., 1969. Introduction to crystallography. WA Benjamin, New York, 165 pp pp.

Teufer, G., 1962. The crystal structure of tetragonal ZrO_2. Acta Crystallographica, 15(11): 1187.